# FIBER-OPTIC SENSING FOR HIGH-TEMPERATURE AND ENERGY APPLICATIONS

by

**Rongzhang Chen**

B.E., Huazhong University of Science and Technology, 2010

Submitted to the Graduate Faculty of

the Swanson School of Engineering in partial fulfillment

of the requirements for the degree of

**Doctor of Philosophy**

University of Pittsburgh

2016

UNIVERSITY OF PITTSBURGH

SWANSON SCHOOL OF ENGINEERING

This dissertation was presented

by

Rongzhang Chen

It was defended on

May 31, 2016

and approved by

Kevin P. Chen, PhD, Department of Electrical and Computer Engineering

Guangyong Li, PhD, Department of Electrical and Computer Engineering

Minhee Yun, PhD, Department of Electrical and Computer Engineering

Susheng Tan, PhD, Department of Electrical and Computer Engineering

Sung Kwon Cho, PhD, Department of Mechanical Engineering and Materials Science

Dissertation Director: Kevin P. Chen, PhD, Department of Electrical and Computer Engineering

**FIBER-OPTIC SENSING FOR HIGH-TEMPERATURE AND ENERGY APPLICATIONS**

Rongzhang Chen, PhD

University of Pittsburgh, 2016

Fiber-optic sensors act as important roles in many of today's industrial sectors. It provides vital information for a large number of applications such as process controls, fossil fuel and nuclear electrical power generation, transportation, and environment monitoring. Compared with their electronic counterparts, fiber-optic sensors truly stand out where extreme operation environments leave almost all the electronic sensors unusable. Derived from the superior properties of optical fibers such as high-temperature stability, immunity to electromagnetic interference and strong resistance to most chemicals, fiber-optic sensors can be engineered to deliver sensing performance under various adverse conditions. Recently numerous research efforts have been put to leverage those merits of optical fibers to achieve sensing capabilities under high-temperature environments ($> 600\,^{\circ}\mathrm{C}$).

In this thesis, five fiber-optic sensing schemes are demonstrated to explore and validate the potential of fiber-optic sensors for high-temperature and energy applications. The first scheme manifests itself as a high-temperature-stable distributed Bragg reflector (DBR) fiber laser which intrinsically is able to operate and measure ambient temperatures up to $750\,^{\circ}\mathrm{C}$.

The second scheme is base on self-heated high-attenuation fibers (HAFs). Thanks to HAFs and regenerated fiber Bragg gratings, a hot-wire flow meter with ambient temperature compensation was realized with all-optical fiber construction with the maximum operational temperature at 800 °C. In the third sensing scheme, the other kind of fiber grating laser,the distributed feedback (DFB) fiber laser as strain sensor is presented to monitor acoustic emissions for a lab-induced hydraulic fracturing process. The ultra-high strain sensitivity of the DFB fiber laser is leveraged the first time to measure the acoustic signals propagated in solid materials. The fourth scheme covers a 3D strain field imaging technique for hydraulic fracturing study, enabled by Rayleigh backscatter based optical frequency domain reflectometry (OFDR). In the fifth scheme, we are aiming at increasing the measurement accuracy of the OFDR system by reducing the system measurement noise level. Via cavity ring down method, the system noise is demonstrated to reduce by over 52%. Such improvement will be instrumental to enhance the OFDR system in measuring small signals. All these technologies and devices offer reliable and flexible sensing solutions for high-temperature and energy industrials, which were not previously possible.

## TABLE OF CONTENTS

## LIST OF FIGURES

## PREFACE

PhD study is the most significant journey in my life. Without the help and support from others, I would not have finished this journey all by myself.

Firstly, I would like to thank Dr. Kevin P. Chen for his constant support and guidance to my study at University of Pittsburgh as my advisor. He imparted with me tremendous knowledge in the area of fiber optics, lasers and photonics both in theory and experimentation. Without his guidance, none of these would be possible. I would also thank Dr. Sun Kown Cho from the department of mechanical engineering and materials science, Dr. Guangyong Li, Dr. Susheng Tan, and Dr. Minhee Yun from the department of electrical and computer engineering for your support and guidance on my PhD program and agreeing to join my program committee.

During years of my PhD study, I have received numerous help, consulting, and collaboration from colleagues in our group and other professors. I cannot name all of them. But a special thank to Dr. Geoffrey Cranch fron Navy Research Laboratory, Prof. John Canning and Dr. Kevin Cook from University of Sydney, and Dr. Tong Chen, Dr. Qingqing Wang, Dr. Botao Zhang, and Dr. Di Xu who all graduated or have worked in our group. I am both grateful and glad that I am in a diverse and dynamic group with so many geniuses around me, from who I can always learn.

Finally, I would like to thank my family members for just being there. Your encouragement and love have helped me conquer challenges both in the study and life.

# 1.0 INTRODUCTION

The early concept of optical fiber was initially proposed around 1940s, reinvented and transformed to its current design in 1960s and then the first time practically manufactured by Corning in 1970. Since then optical fibers quickly evolved to become the backbone of today's network and communication systems. With its almost unlimited bandwidth and low loss properties, optical fiber successfully supplanted copper wire infrastructure and dominated the telecommunications industries. As light waveguides, current optical fibers have nearly addressed the challenge set by the exponentially increased demands for bandwidth of telecommunication 40 years ago. However, it does not mean persistent development of optical fibers and their applications have come to an end. The research efforts nowadays have been more put into opening up new applications and technologies of fiber optics, such as optical fiber sensors and fiber lasers.

Although people can easily obtain various types of off-the-shelf electronic sensors which fulfill tasks fairly well under normal operation conditions these days, the merits and convenience of electronic devices such as relatively high sensitivities, low costs and fast responses quickly degrade as its operation conditions deteriorates. For example, high-temperature environments ($> 200\,^{\circ}\mathrm{C}$) can easily damage the sensor packaging, change conductivity of material and even melt the sensor itself. Also strong electromagnetic interference (EMI)

inhibits sensor control, signal feedback and even permanently break the sensor circuitry. In other words, electronic sensors might incur imminent difficulty in surviving the harsh conditions, not to mention recording data properly. However, fiber-optic sensors are well-known for their resilience in many harsh conditions including in high-temperature, corrosive, and strong electromagnetic environments. With careful engineering, fiber-optic sensors can tackle those adverse environments and accomplish the sensing tasks.

To further extend the territory and unique applications of fiber-optic sensors, I have mainly concentrated on developing five new fiber-optic sensing schemes. Two of them are specially intended to use under high-temperature environments ($> 700\,^{\circ}\mathrm{C}$) and the other two are intended to assist the development of a fast growing field in today's energy industrial, the hydraulic fracturing. As fiber manufacturing technologies quickly matured and leaped forward in the last 40 years, the optical fibers doped with gain media such as erbium and ytterbium were seeing increasing performance and popularity. Combined with the ultra-low loss of optical fiber, optical fiber laser can be achieved if proper cavity is formed. Basically there are two kinds of fiber laser cavities well developed in the research and industrial areas. They are the linear and ring cavities. The latter one literally does not need any reflectors to confine the most energy of light in the cavity but it does need output coupler which can couple part of the laser emission out of the cavity for good uses. For output couplers, we already have fiber coupler readily available. Thus optical fiber ring laser can be made with all-optical-fiber configurations which preserves the optical fiber advantages mostly. Similarly we desire the same all-optical-fiber property from the linear cavity fiber laser as well. Without compromising the integrity of all-optical-fiber configuration, traditional reflectors such as free-space mirrors certainly cannot be employed. To preserve the all-fiber construction

meanwhile providing sufficient quality number for the cavity, the distributed Bragg reflector (DBR) fiber laser is the best candidate. In this thesis, a high-temperature-resistant DBR fiber laser is demonstrated in chapter 3. Contrasted with most conventional DBR fiber lasers which can only operate under ambient temperature less than 200 °C, our proposed DBR fiber laser can stably work and survive 750 °C, beneficial from the thermal regeneration of FBGs. Capable of operating over such a large temperature range, the fiber laser intrinsically can be used as an active temperature sensor and more importantly this demonstration is indicative of the feasibility to enable other already available active fiber laser sensing techniques to work under high-temperature domain.

Flow measurement plays an indispensable role in modern industrials especially for energy applications. In fossil fuel energy industry, there are needs to measure combustion processes that routinely need to measure flows of gases at high temperatures. This information is needed to adjust the injection of fuels to optimize efficiency and to lower the pollutant contents. In nuclear reactors and recent molten salt reactors, there are also needs to measure liquid flows at temperature $> 600\,^{\circ}\mathrm{C}$. Exemplified by all those specific situations, the industrials need a high-temperature-resistant flow meter for their respective applications but they can rarely find proper solutions from conventionally electronic flow meters due to the harsh operational environments. However, fiber-optic sensors seem to be good candidates to fulfill those harsh-environment sensing demands. Thus another active fiber-optic sensor we are going to cover in this thesis in chapter 4 is a high-temperature-resistant flow meter based on self-heated HAFs. The whole fiber sensor was constructed and can be interrogated with single optical fiber, working under hot-wire anemometry with compensation to various ambient temperatures. Thanks to the thermal regeneration of FBGs, the fiber sensor was able to

be characterized to sense flow rates from the room temperature up to 800 °C. Multiplexing capability and distributed sensing are also feasible to further enhance the performance of flow sensor networks.

Energy industrials have always been the cornerstone for sustainable development of today's economy, in which gas and oil production are certainly playing a major role. With increasing level of difficulty in extracting conventional oil/gas resources, the energy industrials have been forced to move to unconventional resources such as shale gas and petroleum. In order to effectively extract gas and oil from resource-bearing shales, hydraulic fracturing technique was developed. Essentially in the hydraulic fracturing process, fluid propellents are injected with high hydraulic pressure to fracture the shale rocks around the wellbore through perforations wherein the natural resources can be released and then extracted. To conduct such process effectively in terms of economy considerations as well as environmental consciousness, extensive study on the behaviors of hydraulic fracturing under different conditions needs to be performed and also the on-site monitoring of the hydraulic fracturing process is highly preferred. To address those demands, in this thesis, I propose two fiber-optic sensing techniques which can add more capability and functions to the currently available tool set for hydraulic fracturing monitoring and diagnosis. In chapter 5, a DFB fiber laser strain sensor was used the first time to measure acoustic emission induced by hydraulic fracturing process. With ulra-high strain sensitivity of the DFB fiber lasers, the intensity of the hydraulic fracturing process is well monitored and the on-site of major breakdown of the sample is effectively predicted. In the following chapter 6, a strain field imaging technique is proposed to provide with civil engineers an extra tool to study the complex hydraulic fracturing process. The technique is enabled by Rayleigh backscatter optical frequency domain

reflectometry (OFDR) method with embedded and specifically shaped optical fibers. The recorded distributed strain data along the fiber is re-mapped in 3D to reveal the strain field inside the concrete sample. We will see that this technique tracks the strain field evolution through the whole hydraulic fracturing process and offer insightful information to determine the possible locations of the first crack that reaches the surface of the sample.

Continuing our application of the OFDR system in the energy fields and also having observed its limitations, we started to think about creating a way to enhance the limit of detection of the OFDR system for strain or temperature measurements while preserving its inherent strength of distrusted measurement. An improved LOD in strain or temperature will be well appreciated in any accuracy-demanding applications and might also open up new applications for this innovative fiber optics sensing technique. Based on the nature of the system noise from the OFDR system, a cavity ring down configuration was proposed to work with the OFDR system. The goal is to reduce the system noise level to improve the limit of detection by simultaneously conducting multiple measurements all at once. Therefore random components in the system noise can be canceled out statistically. In chapter 7, we will first in detail discuss the cavity ring formation, its design and special considerations. And then we will look into the unique way that OFDR system uses to interrogate such a relatively high-finesse cavity. Lastly, actual temperature measurements obtained with the proposed method will be presented and the system performance enhancement will be discussed.

# 2.0 SENSOR DESIGN

One major sensing concept in this thesis is based on fiber Bragg gratings (FBGs). We employed its wavelength-selected reflectivity to make fiber lasers and its high sensitivity on temperature changes to sense flow rates. Both sensing techniques were intended for high-temperature environments ($> 750\,^{\circ}\mathrm{C}$). To make FBGs high-temperature-resistant which normally degrades rapidly after $200\,^{\circ}\mathrm{C}$, we used thermal regeneration to form high-temperature-stable FBGs. To better discuss our sensing concepts, we are going to briefly introduce the concept of FBGs and the thermal regeneration process. Then we focus on specific sensor designs and their operating mechanism.

## 2.1 FIBER BRAGG GRATING SENSORS

### 2.1.1 Overview

The first ever fiber Bragg grating (FBG) was discovered by Hill *et al* in 1978 [1] when they guided emission of an Argon laser of 488 nm into a piece of germania doped optical fiber and then found out that the reflected laser light at the input port increased with the exposed time. It was found out that the laser emission formed a standing wave inside the

optical fiber between the input laser light and the reflection from the fiber end face and such standing wave varied the local refractive index of the optical fiber accordingly. Due to the sinusoidally modulated refractive index in the optical fiber, the first FBG was formed somehow "accidentally". Later research efforts showed that it was due to the two-photo absorption of germania doped optical fiber at 488 nm that changed the refractive index [2]. However, due to the fabrication methods that directly depended on the interference of the laser light, the FBGs at that time could only cover visible spectral range, which unfortunately precluded any practical uses of FBGs in telecommunication whose operating wavelengths were in infrared ranges. The situation was not changed until the revolutionary holographic writing of gratings was proposed by Meltz *et al* [3]. They used a 248 nm excimer laser and an interferometer to form coherent UV interference pattern on the side of the optical fiber. By single-photon absorption of the oxygen-vacancy defect band of germania at 244 nm, a FBG was inscribed within visible wavelength with ∼50–55% reflectivity. Even though their demonstrated results were still within visible wavelength range, the method of fabricating FBGs truly opened up new era for prosperous FBGs applications. By tuning the coherent UV interference pattern which was not attainable before, people could readily extend the operating wavelength of FBG into telecommunication regimes [4]. Besides the breakthrough on how FBGs could be better and flexibly made, another development again pushed its applicability to a new level. Much stronger gratings can be inscribed with hydrogen-loaded optical fibers [5], which makes some of the reflectivity sensitive applications possible and much more feasible than ever before such as fiber lasers with linear cavities and even high-power lasers.

### 2.1.2 Photosensitivity

Photosensitivity literally refers to permanent refractive index changes of optical materials under influence of light illumination. Refractive indices describe the reactions between the materials and the light propagating inside. According to classic electron model [6], the light travels inside the materials in the form of electromagnetic waves, alluding to its interaction with dipoles which are composed of positively charged atomic nuclei and negatively charged electrons around it. The electrical field drives both types of charges up and down, acting as driven harmonic oscillators. Due to large mass difference between the atomic nuclei and electrons. The movement of electrons play major roles. Thus the induced dipole displacement can be described as

$$D = \epsilon_0 E + P \tag{2.1}$$

where $\epsilon_0$ refers to the permittivity in the free space, E is the applied field and P indicates the induced polarization. Due to the nonlinearity inside the materials, induced polarization has its first order linear term, second order nonlinear term and third order and so on.

$$P = \epsilon_0 \chi^{(1)} E + \epsilon_0 \chi^{(2)} E^2 + \epsilon_0 \chi^{(3)} E^3 + \dots \tag{2.2}$$

In the (2.2), $\chi^{(2)}$ is the second order nonlinear susceptibility and $\chi^{(3)}$ is the third order susceptibility. By combining (2.1) and (2.2), we arrive at,

$$D = \epsilon_0 E(1 + \chi^{(1)} + \chi^{(2)} E + \chi^{(3)} E^2 + \dots) \tag{2.3}$$

We define,

$$\epsilon_r = 1 + \chi^{(1)} \tag{2.4}$$

Then (2.3) can be further reduced to

$$D = \epsilon_0 E(\epsilon_r + \chi^{(2)}E + \chi^{(3)}E^2 + \ldots) \tag{2.5}$$

For the situation with low-intensity light propagating inside low-nonlinearity materials, higher-order nonlinear effects can be neglected such as $\chi^{(2)}$ and $\chi^{(3)}$. Thus the refractive index is easily defined as,

$$D = \epsilon_0 \epsilon_r E = \epsilon E = n^2 E \tag{2.6}$$

where $\epsilon$ refers to the permittivity of the material and $n$ is the refractive index.

There are a lot of mechanisms which has been discovered to induce index changes permanently, including UV exposure, ultrafast laser direct writing, poling. Different methods are based on various physics in the materials. Even though the nature of photosensitivity of optical materials such as silica glasses is still under debating and continuously being developed, we do have some mostly accepted points of view to explain at least part of the picture in terms of photosensitivity.

UV exposure is one of the most matured techniques used to modify materials' refractive indices on demand and also the method we took in this thesis. It has been widely used to fabricate FBGs commercially and also in laboratories. For this method, the defects in the optical fiber played significant roles to react with the incoming laser exposure. Defects such as Ge oxygen deficient centers (GeODC) contributing to optical fiber photosensitivity can be naturally formed in the fiber cores during the process of optical fiber fabrication [7], which is quite brutal in a microscopic perspective. In addition a reduced ambient such as high-temperature hydrogen treatment during fiber drawing process can also produce more GeODCs [8]. The existence of GeODC with UV exposure can modifies the local structure of

the material in terms of volume, strain and also absorption properties, resulting in refractive index changes. Such reaction is shown in Fig. 1, where by breaking the Ge-Si bond via single photo absorption 240 nm UV exposure can reduce the Ge states, liberate an electron and form the GeE' defect inside the optical fiber cores [9]. The formation of the defect deforms the structure of Ge and thus modify the refractive index locally.

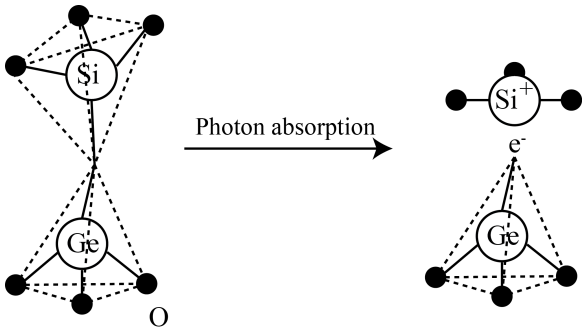


Figure 1: UV illumination upon a GeODC in germanium-doped optical fibers.

Hydrogenation is another well established photosensitization methods [5]. With the help of hydrogenation, the UV exposure methods produced the highest refractive index modulation in germanium-doped optical fibers. When the optical fibers are soaked in cold/hot high-pressure hydrogen environments, the hydrogen molecules diffuse into the fiber cores until an equilibrium state. Upon UV illumination, the hydrogen molecules are dissociated to form Ge-OH or Si-OH bands and GeODCs which directly contribute to the refractive index changes with further UV exposures. Besides, with molecular hydrogen existing inside the optical fiber core and UV radiation, formation of GeH and GeOH ions can be triggered as well [9], as shown in Fig. 2. The resultant GeH changes the local refractive index via Kramers-Kronig rule. In the experimental procedure demonstrated in this thesis, we used 165 bar hydrogen bath of 1 week at room temperature to enhance photosensitivities of the

optical fibers employed. In addition to efficiently enhancing the photosensitivity of the optical fiber, hydrogenation process is versatile. This treatment can photosensitize almost all kinds of germanium-doped optical fibers even those erbium-codoped gain fibers.

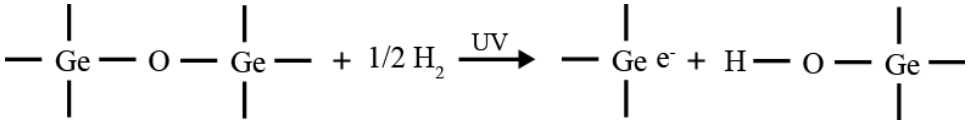


Figure 2: Enhanced GeH defect formation in hydrogen-loaded optical fibers.

Ultrafast laser direct writing is another class of techniques used to permanently change refractive indices of optical materials. Its popularity and practicality is developing rapidly with the increasing performance of modern ultrafast laser system and nanometer-accuracy motion stages. The optical materials are generally transparent from visible wavelength up to near infrared wavelength range. However, this situation does not hold when femtosecond pulses are propagating inside the optical materials. Due to the nonlinearity of the optical materials under high-intensity laser pulses, optical materials start to behave as opaque materials, which absorbs photon energies to generate heat. Since the laser pulses are ultrafast on the level of tens of femtoseconds, the heat generated by photon absorption is usually too efficient to be dissipated of the materials and is given as energy to lattices. Thus local high-temperature environments are induced and it gives rise to the onsite of strong plasma emission, which results in dielectric breakdown and catastrophic damages. Ultrafast laser direct writing has been used to write FBGs in optical fibers as well [10, 11]. They are generally high-temperature resistant ($> 1000\,^{\circ}\mathrm{C}$) due to the nature of grating formation [12]. However, they also suffered from other side effects such as fragility and inferior spectral quality.

Poling is also manifested as photosensitivity of optical materials. Unlike generating defects or inducing damages to permanently change the refractive indices of materials, poling leverages recorded internal DC electrical fields to change refractive indices by introducing or enhance its nonlinear susceptibilities. Continued with the (2.5), we define,

$$\Delta\epsilon = \chi^{(2)}E + \chi^{(3)}E^2 + \dots \tag{2.7}$$

Those nonlinear coefficients are usually small but cannot be neglected when light propagating has high intensity or optical material has been modified with strong recorded DC electrical field, where poling takes effects. Since nonlinearity modifies refractive indices of optical materials under influence of strong electrical fields, we describe the refractive index changes as below,

$$\epsilon = (n_0 + \Delta n)^2 = n_0^2 + 2n_0\Delta n \tag{2.8}$$

where $n_0$ indicates the refractive index of the material and $\Delta n$ is the induced change. Compare (2.8) and (2.6) with (2.5), we have

$$\Delta n = \frac{(\chi^{(2)}E + \chi^{(3)}E^2 + \dots)}{2n_0} \tag{2.9}$$

From (2.9), the linear electro-optic effects via $\chi^{(2)}$ is clearly pointed out. Even though in amorphous or crystalline materials like fused silica there is no second-order nonlinearity existing due to the lattice symmetry, we can still use fiber poling techniques [13] to produce effective $\chi^2$, which enables the useful electro-optic effects in optical fibers. Based on such property a phase modulator can be fabricated [14]. More interestingly, second order harmonic generation (SHG) which relies on $\chi^2$ has also been demonstrated based on third-order mixing and thermal poling [15]. In silica glass, (2.9) can be further reduced to

$$\Delta n = \frac{(\chi^{(3)}E^2 + \dots)}{2n_0} \tag{2.10}$$

Then if we consider a large recorded $E_{DC}$ already established inside the material and a relatively small $E_{sig}$ applied externally, we derive,

$$\Delta n = \frac{\chi^{(3)}}{2n_0}(E_{DC}^2 + 2E_{DC}E_{sig} + E_{sig}^2) \tag{2.11}$$

where other higher order nonlinear susceptibilities have been neglected. The equation above (2.11) partly serves as the foundation of fiber poling and SHG in fused silica fibers.

### 2.1.3 Grating Formation and Fabrication Method

Fiber Bragg gratings (FBGs) are formed by sinusoidal modulation of refractive index in optical fibers. Different UV exposure methods have been proposed to induce such modulation including the interferometer method [3], the phase mask method [16], and the scanning interferometer method [17]. Those methods are capable of providing various advantages and flexibilities on fabricating FBGs. However, all of them share the same core idea that the interference pattern produced by two beams spatially overlapped is used to induce the similar index modulation pattern in the fiber cores.

After UV exposure applied, the modulated refractive index of the optical fiber after illumination can be described as,

$$n(z) = n_0 + \Delta n \sin\frac{2\pi}{\Lambda}z \tag{2.12}$$

where $n_0$ is the DC component of the refractive index modulation, $\Delta n$ indicates the modulation depth after UV exposure, and $\Lambda$ is the modulation period. Thus we can derive the modulated permittivity as,

$$\epsilon_0 n^2(z) = \epsilon_0 n_0^2 + \epsilon_0 2n_0\Delta n \sin\frac{2\pi}{\Lambda}z \tag{2.13}$$

We neglect the high-order term of $\Delta n^2$, and consider $\epsilon(z) = \epsilon_0 + \Delta\epsilon(z)$

$$\Delta\epsilon(z) = \epsilon_0 2n_0\Delta n \sin\frac{2\pi}{\Lambda}z \tag{2.14}$$

At this point the fourier component can be directly identified as,

$$\epsilon_1 = 2\epsilon_0 n_0 \Delta n \tag{2.15}$$

Thus, its coupling coefficient can be derived,

$$\kappa = C^{(1)} = \frac{\omega^2\mu}{2\beta}p'\epsilon_1 p = \frac{\omega^2\mu\epsilon_0 n_0}{2\beta}\Delta n = \frac{\pi}{\lambda}\Delta n \tag{2.16}$$

According to coupled mode theory, the reflected light wave coupled from incident light wave under perturbation of FBG can be described as,

$$R = \frac{|\kappa^2|\sinh^2 sL}{s^2\cosh^2 sL + (\frac{\Delta\beta}{2})^2\sinh^2 sL} \tag{2.17}$$

$$\Delta\beta = 2\beta - m\frac{2\pi}{\Lambda} = \frac{2n_{eff}}{c}(\omega - \omega_0) \tag{2.18}$$

with parameter $s = \sqrt{|\kappa|^2 - (\frac{\Delta\beta}{2})^2}$, L is the length of the FBG, $\omega_0$ is the center frequency where the Bragg condition is satisfied. The maximum reflectance occurs at $\Delta\beta = 0$, where we get

$$R_{max} = \tanh^2|\kappa|L \tag{2.19}$$

In addition, the spectral width of the photopic bandage can be estimated based on the condition $-2|\kappa| < \Delta\beta < 2|\kappa|$ where strong energy exchange between the forward-propagating wave and contradirectional wave can occur. The estimation is derived below,

$$\Delta\omega_{gap} = 2\frac{|\kappa|c}{n_{eff}} \tag{2.20}$$

Based on the theoretic model indicated above, a 1-cm uniform FBG with resonance peak at 1550 $nm$, $\Delta n = 0.1, 2, 5, 10 \times 10^{-4}$ can be predicted respectively. The simulated results are shown in Fig. 3. With a certain length of FBG, the grating strength is correlated with the refractive index modulation depth $\Delta n$. In terms of absolute strengths for FBGs, a very small depth of modulation $\Delta n = 2 \times 10^{-4}$ can already provide over 99.5% reflectance which is usually sufficient for most of telecommunication needs. However, with hydrogenation and 193-nm UV exposure, $\Delta n = 16 \times 10^{-4}$ has been demonstrated, which is indicative of a grating with over 120 dB in strength [18]. Furthermore, a linear phase shift can also be observed inside the photonic bandgap. This property has been widely used for dispersion compensation applications.

In this thesis, the method we took to produce the aforementioned refractive index modulation is the phase mask method. We leverage a phase mask to act as the beamsplitter and place the optical fiber right after, where two split beams can be spatially overlapped and produce the interference pattern of UV light. A schematic Fig. 4 is shown below to present the formation and operation of the grating inscription system. The 248 nm laser emission is emanated from a GSI Lumonics excimer laser (PulseMaser PM-848). Two UV mirrors are employed to align the laser beam. Since the laser emission out of the exciter laser suffers from relatively high diffraction, non-uniform beam profile and also low time coherence, we utilize an aperture to make use of only the central part of the beam, intending to overcome or at least minimize those negative effects of the original beam. After the aperture, an optic expander is used to increase the usable beam size, which enables us to write different lengths of FBGs with the following variable spatial filter. The laser beam with desired size is focused onto the phase mask by a cylindrical lens with focus length of 10 inches. Finally, a highly

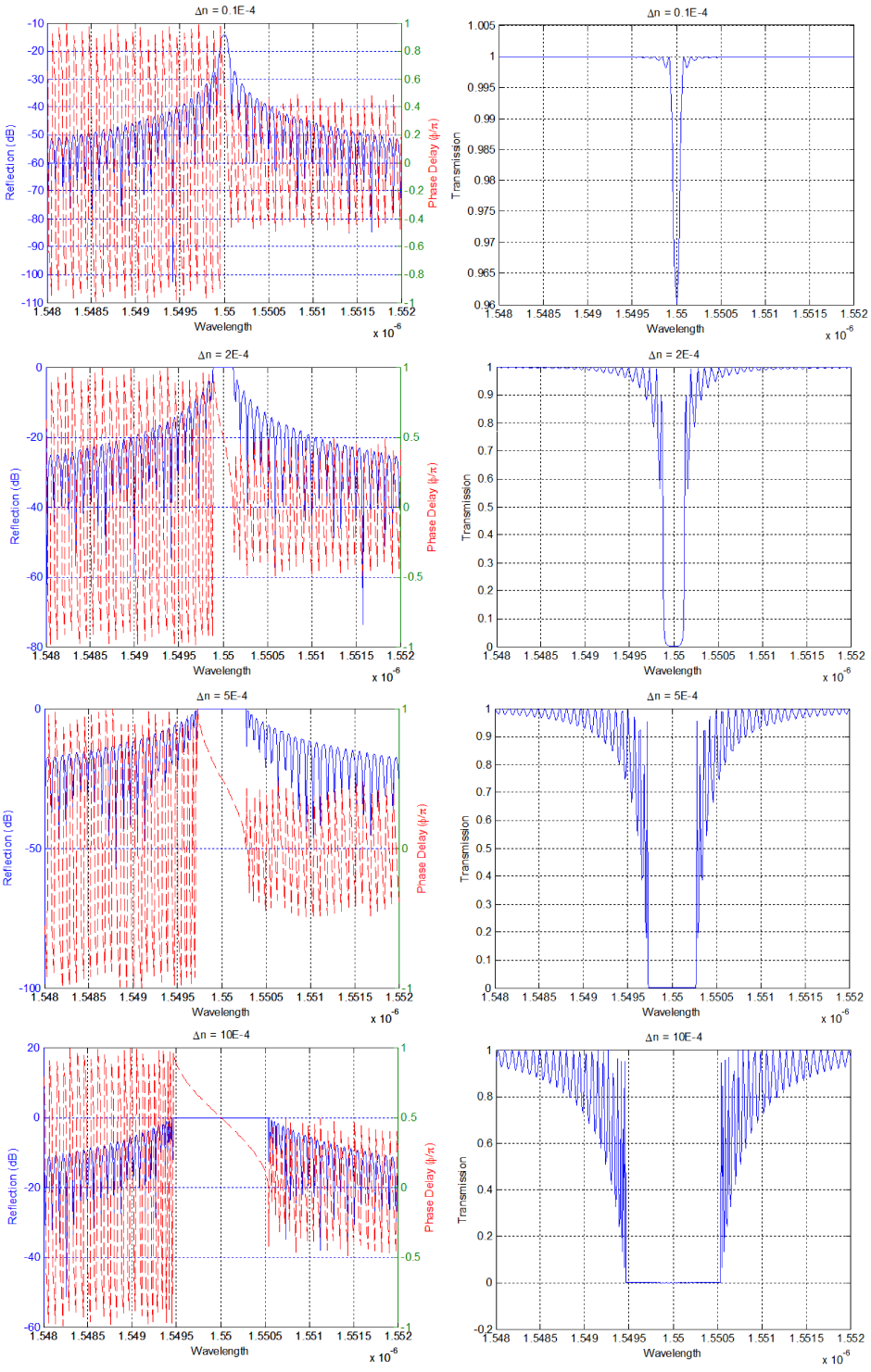


Figure 3: Simulations for 1-cm uniform FBGs with varied $\Delta n$.

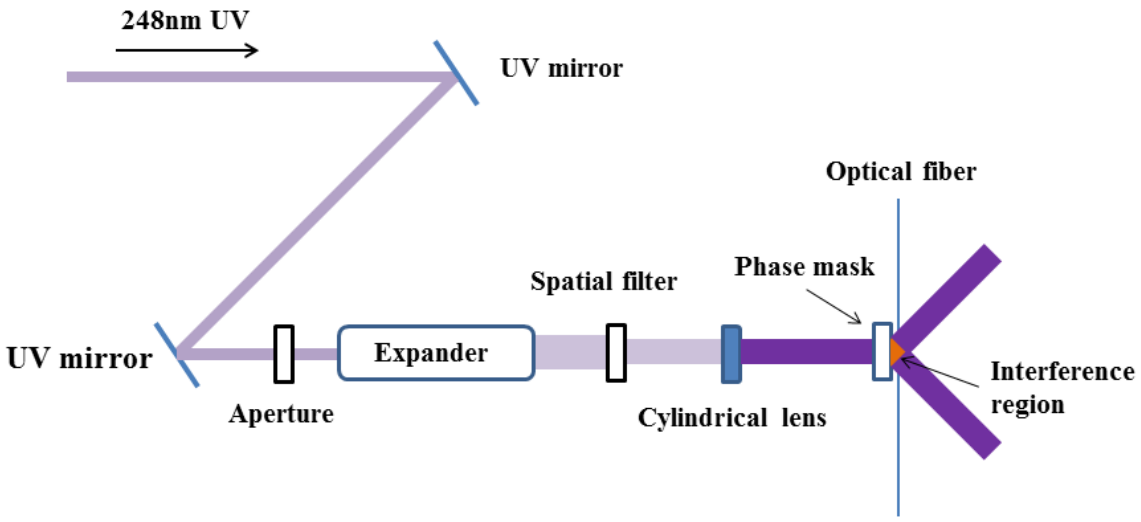


Figure 4: Schematic for FBG inscription setup.

focused interference region is produced behind the phase mask. To take full advantage of the region, we need to place the optical fiber right after the phase mask. FBG shall be inscribed in the core of the optical fiber wherever it is in the interference region. Two photos taken on the inscription setup are also enclosed. In Fig. 5, we can see the phase mask, the cylindrical lens and the variable spatial filter from the near to far views. The optical fiber during the inscription process is fixed by a fiber bench and accurately positioned right behind the phase mask with 6-axis motion stage. Fig. 6 presents the image of two overlapped UV laser beams on a white screen. Even though the 248 nm UV is in the invisible range, the pattern shown on the screen is visible and derived from associated fluorescence during the lasing. Therefore the observed pattern is still a good indicator to show the spatial overlapping of the two UV laser beams.

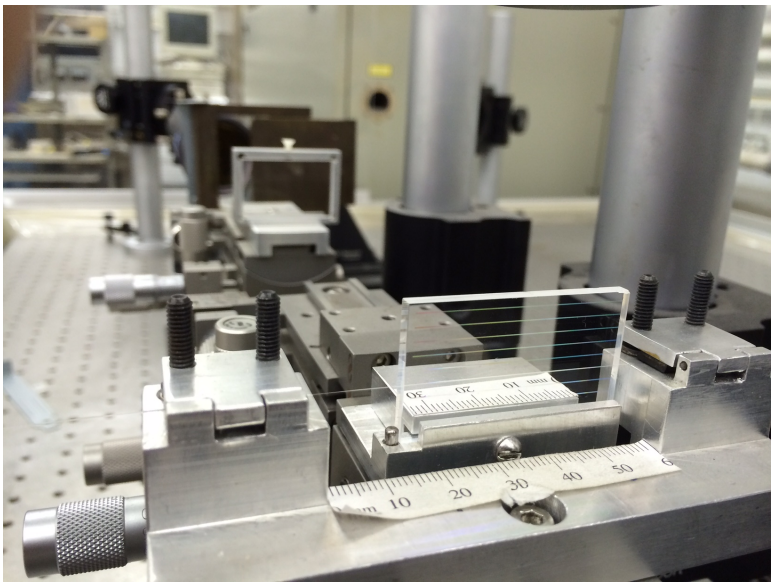

Figure 5: Photo taken on an optical path of the FBG inscription setup.

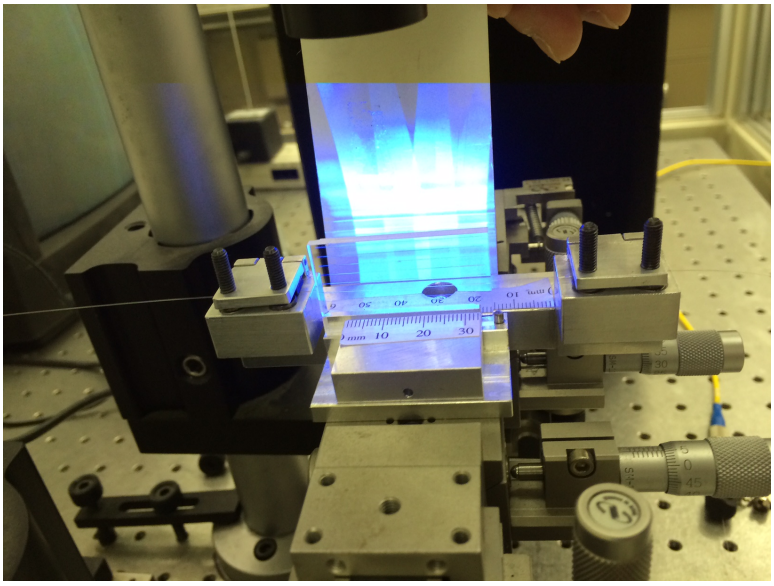

Figure 6: Two split beams are overlapped spatially after the phase mask.

## 2.2 THERMAL REGENERATION

The thermal regeneration of type I grating in high-temperature annealing process was first observed and then confirmed with different groups in the world previously [19–21]. Thermally regenerated gratings are categorized as another class of high-temperature-resistant fiber gratings. The thermal regeneration of high-temperature-resistant gratings involves a mechanical relaxation process [22], which is independent from the chemical composition of fibers and hydrogen loading processes. Thus, thermally regenerated gratings can be fabricated in a wide variety of fibers at low cost for extreme environments. Canning et al has reported linear temperature and strain responses in thermally regenerated gratings from room temperature to 1100 °C [23], which render regenerated gratings as a significant enhancement to conventional fiber grating applications, especially for extreme environments. Recently, we have already demonstrated a regenerated grating based high-temperature pressure sensor, with which hydrostatic pressure 15-2400 psi and high temperature ($24 - 800\,^{\circ}\mathrm{C}$) can be accurately measured simultaneously [24].

Here we are showing a typical thermal regeneration process occurred in a telecommunication optical fiber SMF-28 at 800 °C. In Fig. 7 (a), we observe small reflectance growth at the beginning of the thermal process, indicating annealing out of a negative contribution from UV-induced refractive index modulation [23]. Thereafter the grating strength incurs an exponential decay to its minimum until the onset of grating regeneration is observed. The thermal processing recipe is set at $200\,^{\circ}\mathrm{C}/min$ from the room temperature to 800 °C. The regenerated grating strength continues to increase until it is totally stabilized at its current ambient temperature (800 °C). The fully regenerated FBG is weaker in its grating peak

strengh than its seed grating. By fine tuning the thermal recipe, post-hydrogen loading and of course inscribing strong seed FBGs, the regenerated FBGs with useful strong strengh can be achieved [18]. After the thermal regeneration process, the regenerated FBGs (RFBGs) behave highly temperature-resistant, capable of standing ambient temperatures up to the temperature point where it is treated. Fig. 7 (b) shows the wavelength change of the grating peak during the regeneration process. Besides the red shift of the grating peak during the heating process, we can also observe an limited blue shift as well after the regeneration temperature (800 °C) is established. This is attributed to the thermal relaxation of UV-induced $\Delta n_{DC}$. After that, the peak wavelength of the regenerated grating is stable through the rest of the regeneration process.

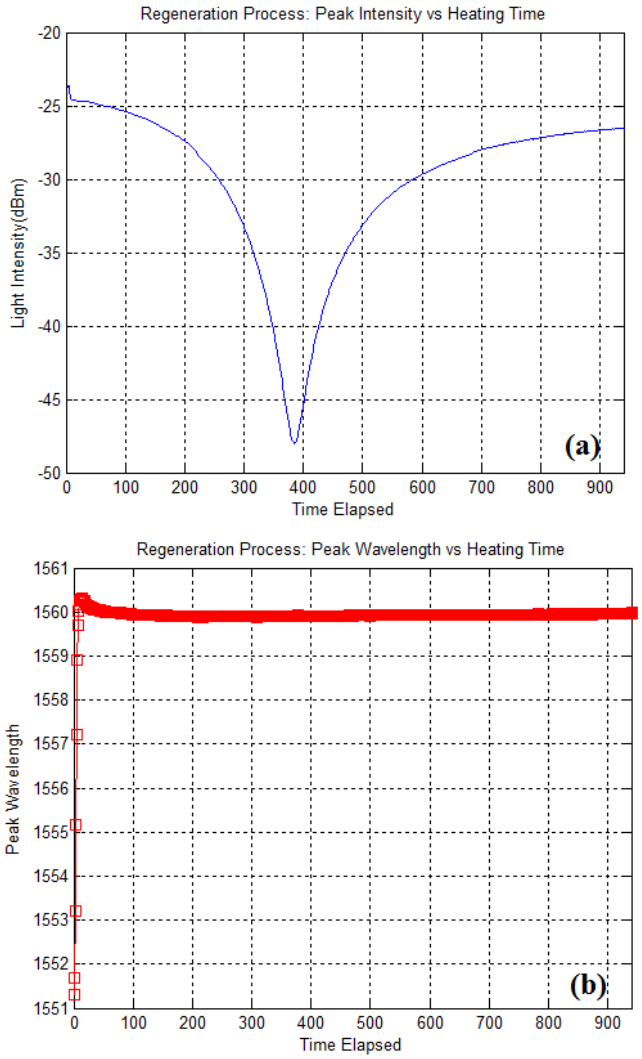


Figure 7: Changes of (a) grating strength and (b) resonance wavelength during the regeneration process.

## 2.3 DBR FIBER LASERS

Given the superior properties that fiber Bragg gratings have to offer, one of the most intuitive ideal about applications is to take full advantage of their sharp bandwidth and high reflectance to make fiber lasers. DBR fiber laser is just an easy embodiment of the idea. By using two FBGs whose peak wavelengths are matched on both sides of the linear cavity and a section of gain fiber in the middle, a simple construction of DBR fiber laser can be made, as shown in Fig. 8. In this figure, the DBR fiber laser is based on erbium doped gain fiber, enabling its laser operation at C band around 1550 nm. A 980 nm laser diode is used to pump the gain fiber through a wavelengh division multiplexer (WDM). The laser emission is then guided to an optical spectrum analyser (OSA) for emission characterization.

Even though DBR fiber lasers are relatively not hard to fabricate, there are still some design considerations worth mentioning. The first one is about single wavelength operation. Based on linear cavity configuration, multiple laser lines can be allowed to exist in the cavity as long as they satisfy the phase matching condition,

$$\lambda = \frac{2}{m}(n_{eff}L) \tag{2.21}$$

where $\lambda$ indicates the lasing mode allowed, $m$ is the mode number, and $n_{eff}$ is the effective refractive index in the cavity. We take a total derivative of both sides of (2.21), we can derive the approximated mode spacing,

$$\delta\lambda = \frac{\lambda^2}{2(n_{eff}L_{eff})} \tag{2.22}$$

According to (2.22), a DBR fiber with $\delta\lambda = 0.05nm$ which is a feasible value for 3-dB bandwidths of FBGs with reflectance over 95% and $n_{eff} = 1.4682$, we can calculate the

minimum cavity length to ensure single wavelength operation, or in other words high side mode suppression ratio. The result indicates $L_{eff} < 16.4\ cm$. As long as this condition is satisfied, the mode space for such cavity is larger than the 3-dB bandwidth of FBG reflectors such that all other side modes are not sustainable inside the cavity due to large cavity loss. As for the effective cavity length, special attention has to be paid as well when it comes to calculation of effective lengths of the two FBG reflectors. Based on effective mirror model for gratings, we have,

$$L_{eff} = \frac{1}{2\kappa} \tanh \kappa L_g \tag{2.23}$$

where $\kappa$ refers to the coupling coefficient and $L_g$ is the respective length of the FBG. The (2.23) can only be applied to the photonic bandgap of the grating where linear dispersion is preserved. Considering the penetration depths of both FBG reflectors on the sides, the total effective length $L_{eff}$ is equal to the sum of the two penetration depths of the FBGs and the length of the gain fiber in the middle.

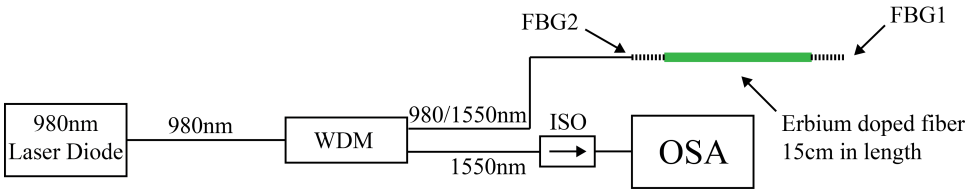


Figure 8: Typical configuration of a DBR fiber laser and its characterization setup.

Fiber lasers are powerful tools for sensing applications. Numerous research efforts have been demonstrated to apply DBR fiber lasers into different sensing scenarios, including lateral force measurements [25],simultaneous refractive index and temperature measurements [26], high-resolution strain and displacement sensing [27, 28],and even ultrasonic detection [29].Compared with passive fiber Bragg gratings, active sensing schemes based on

fiber lasers normally show superior performance in terms of sensitivity, frequency response and accuracy. Recent research efforts have extended the operational temperature of fiber lasers to (600 °C) for high-temperature harsh environments [30]. This is well beyond those prescribed for classic applications such as telecommunications. The successful development of all-fiber high-temperature fiber lasers relies on high-temperature-resistant fiber Bragg reflectors. In view of those requirements, FBGs inscribed by ultrafast lasers, at the first place, have been proved to be promising candidates. For example femtosecond laser inscribed Type II gratings were successfully used in fiber lasers operating at temperature up to (600 °C) [30] and output power scaling to 103W [31], thanks to their high-temperature stability and subsequent power handling capability. Conventional UV-inscribed Type I fiber gratings are typically less temperature-resistant than those fabricated by femtosecond lasers. Annealed UV-inscribed fiber gratings in photosensitive fibers, with much simpler fabrication process and less costs, can sustain lasing up to (400 °C) [32].

In addition to passive sensing applications, regenerated gratings can offer considerable potential for applications in high-power laser [31] and active fiber sensing areas, where internal temperatures of fiber lasers can anneal conventional gratings out under high laser output power. With specially optimized optical fibers and strong seeds, regenerated gratings with 98.5% reflectance ($\sim 18dB$) can be readily fabricated [18], which is normally sufficient for laser oscillation with a relatively small cavity size.

In the next chapter, we will in detail discuss the research efforts we put in the development of high-temperature-resistant DBR fiber lasers by leveraging thermally regenerated FBGs as reflectors. Beneficial from the high-temperature resistance of RFBGs, the demonstrated RDBR fiber laser can sustain lasing at (750 °C) for 7 hours with no performance

degradation. The index modulation of the regenerated grating might also be sufficient to produce distributed feedback laser with much better longitudinal mode stability. The thermal regeneration FBG fabrication process opens new possibilities to design and implement fiber laser sensors for extreme environments.

## 2.4 DFB FIBER LASER STRAIN SENSOR

### 2.4.1 Overview

As mentioned in the previous section, DBR fiber lasers are revealed as superior platforms to carry out a variety of sensing experiments. However, they are still limited by couple of aspects in terms of laser stability and resistance to environmental perturbations. For example, the laser wavelength out of a DBR fiber laser will be subject to the relative separation of the Bragg gratings where mode hopping or multi-mode operation can both occur and also environmental perturbations can as well influence the stability of a DBR fiber laser since relatively longer effective cavity length (normally couple of centimeters level). Improving from the DBR fiber laser design, a more stable cavity can be achieved by incorporating a $\frac{\pi}{2}$ phase shift into a fiber Bragg grating inscribed on a rare earth metal (Er and Yb) doped optical fiber. The simulated cavity characteristics are shown in Fig. 9 below. This kind of fiber lasers are therefore called distributed feedback (DFB) fiber lasers since the optical gain is distributed along the FBG, unlike in DBR fiber laser configurations where the two FBGs are both passive.

In Fig. 9, beneficial from the introduced $\pi/2$ phase shift either done by shifting the refractive index modulation or post processing after grating inscription, a sharp dip at the center of the band gap of the FBG is observed in the aforementioned reflection spectrum, indicative of the cavity formation in the grating. Such cavity nature can be more easily visualized by the group delay plot, where a pronounced increase in group delay at the center of the band gap is on site. The high group delay value corresponds to one longitudinal mode at the Bragg frequency that is only allowed in such cavity, guaranteed by the phase matching

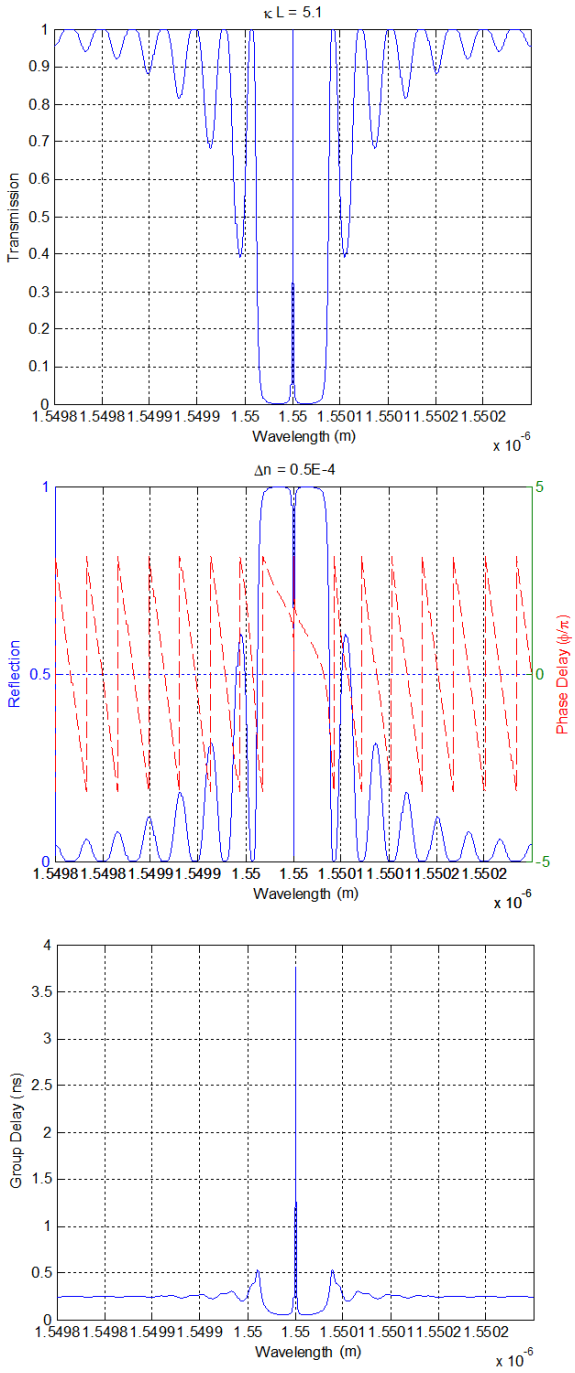


Figure 9: Transmission, reflection spectra and group delay of a 5-cm-long $\frac{\pi}{2}$ phase shift grating with $\kappa L = 5.1$.

condition. When sufficient gain is provided through optical pumping along the FBG, the single-longitudinal-mode is achieved provided the in-cavity net gain or the FBG strength is not too strong. By employing apodization to convention uniform grating structures, the suppression to side lasing modes of the DFB fiber lasers can be further enhanced [33]. As presented by the simulation results in Fig. 10 below, we applied a gaussian shaped apodization to a 5-cm-long uniform grating index modulation such that the average refractive index modulation $n_{eq} = 0.5e - 4$ is still preserved according to those shown in Fig. 9. The group delay of the apodized phase shift FBG is greatly enhanced by almost 10 times plus narrowed overall band gap of the grating, both of which contribute to higher lasing thresholds for side longitudinal modes. It is also worth noting that the phase-shifted feature is not truly required for DFB fiber lasers to lase but indispensable in ensuring its lasing that only takes place at the fundamental mode or the Bragg wavelength. For unshifted DFB fiber lasers, the Bragg wavelength does not support any lasing solution due to the mismatch of the phase. However, two adjacent longitudinal modes with equal spectral distance on the left and right of the Bragg wavelength can reach lasing threshold simultaneously. Therefore the single-mode operation cannot be obtained in unshifted DFB fiber lasers.

### 2.4.2 Fabrication

In the fabrication phase, DFB fiber lasers can be most likely made in the same way as uniform FBGs are fabricated except that the grating structures are to be inscribed on gain fibers instead of passive ones and a $\frac{\pi}{2}$ phase shift needs to be processed with full attention. Different techniques have been proposed so far to induce such specific phase shift, which generally includes UV-post processing [34], dithering of the scanning laser beam [35,36] and

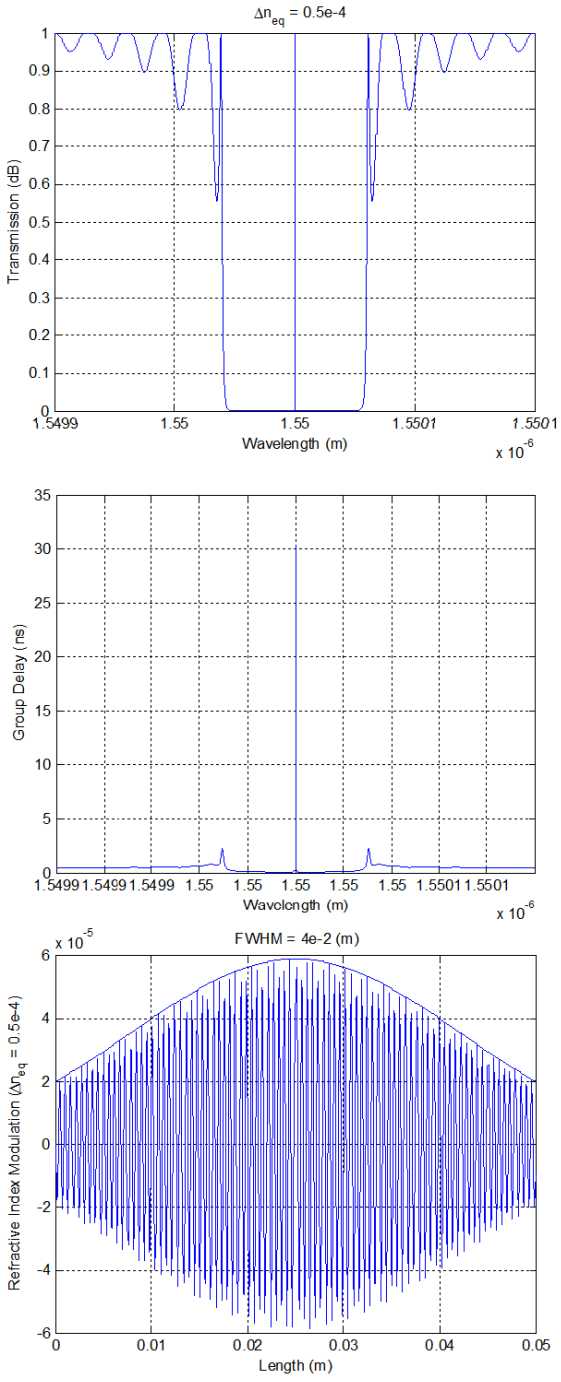


Figure 10: Transmission, group delay and apodization of a 5-cm-long $\frac{\pi}{2}$ phase shift grating.

of course the most direct way, translation of optical fiber by motion stages to induce the overlapping between two composing FBGs [37].

Intrinsically speaking, all the three methods mentioned above are aimed at modifying $\Delta n_{DC}$ locally such that the phase shift over the processed section is equal to $\frac{\pi}{2}$. For example, in UV-post processing, usually a several-millimeter-long section of the optical fiber at the center of the inscribed FBG is exposed to UV illumination for the post processing. Such extra dosage elevates the local $\Delta n_{DC}$ to a value where the desired phase shift is achieved. In scanning interferometer method, the dithering of the laser exposure at a certain length of the FBG play a significant role to increase $\Delta n_{DC}$ locally, therefore, to induce the extra phase shift. The most straight forward way to generate DFB structures belongs to translation of the two composing FBGs in the optical fiber. Practical translation distance between the two FBGs is generally less than one grating period, which at the same time requires high resolution (nm-level) of the translation stages employed.

### 2.4.3 Strain Measurements and Interrogation

Beneficial from the stable single longitudinal mode operation, DFB fiber laser have been proved to be among the most sensitive strain sensors that photonics technology can offer [38]. With proper wavelength decoding method, the DFB fiber laser can resolve length changes as high as $0.76fm/Hz^{1/2}$ at 2 kHz, which is equivalent to $117f\epsilon/Hz^{1/2}$ given an effective cavity length of $L_c = 6.5mm$. With such high strain sensitivity, DFB fiber lasers have been largely introduced in acoustic measurements recently, especially for hydrophone applications [39]. In the scope of this dissertation, we look into applying DFB fiber lasers in measuring acoustic signals propagating in solids with frequency under 250 KHz. The upper frequency range

is limited by sampling rate of the analog to digital converter. For acoustic waves in this frequency range (DC to 250 KHz), their wavelengths are generally much larger than the length of effective cavity of the DFB fiber laser, approximatedly as 10 mm. Thus axial strain can be always treated as longitudinally uniform when the acoustic waves propagate through the mounting material of the fiber laser or the laser itself [40]. Under this condition, the characteristics of DFB fiber laesr under axial strain has become very similar to that of conventional FBGs. The frequency change of the fiber laser is governed by

$$\Delta\nu/\nu = 0.78 \cdot \Delta\epsilon \tag{2.24}$$

in which 0.78 accounts for the strain-optic coefficient [41].

To achieve such level of strain or displacement sensitivity mentioned above is never trivial, which requires highly sensitive laser frequency discrimination capability. In this dissertation, we use the passive homodyne interferometry based on $3 \times 3$ coupler to interrogate the frequency shift of the DFB fiber laser under tests [42]. This method is well known for its real time acquisition capability and wide range of frequency responses. Other than this method, there are other two methods worth mentioning: the active homodyne [43] and the heterodyne phase-generated carrier (PGC) [44]. Intrinsically, the three methods are very similar in ways that they all involve interferometry configuration which are actually very essential in wavelength interrogation here. By using the interferometers, the wavelength change of the laser can be converted to the phase change at the output of the interferometer based on the measurement of light intensity. The imbalanced optical path in the interferometer produces equivalent optical gain to convert and amplify the frequency shift into the phase shift. The difference between the three techniques is noted by where the phase shift can

be properly interrogated. With $3 \times 3$ coupler as the output coupler of the interferometer, the optical phase is calculated in real time based on the inherent phase difference between the three outputs of the $3 \times 3$ coupler. In active homodyne method, a PZT is employed in one arm of the interferometer to maintain the optical phase always shifting around its quadrature such that the phase values are proportional to the light intensity at the output of the interferometer. Lastly for heterdyne phase-generated carrier technique, a PZT is again involved in one arm of the interferometer. Instead of being used to compensating for any environmental noises as it does in active homodyne method, it is now used to generate the high frequency phase modulation. The output signal of such phase modulated interferometer is subsequently analyzed by spectrum analyser in frequency domain, where strain induced phase change can be extracted.

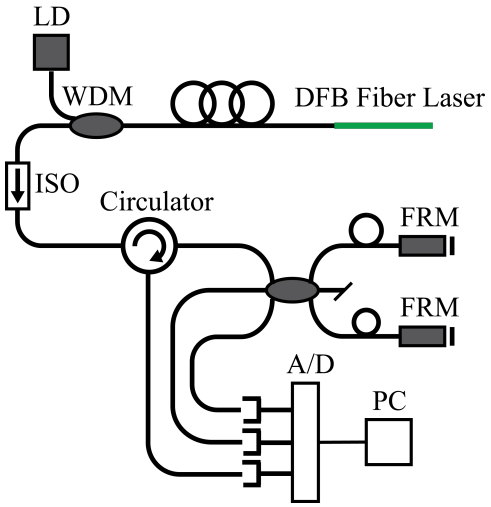


Figure 11: DFB fiber laser sensor interrogating configuration.

The configuration of the $3 \times 3$ coupler based interrogation system is shown above in the Fig. 11. The DFB fiber laser is pumped with a 980 nm laser diode (LD) at 200 mW and a wavelength division multiplexer (WDM). The laser output is guided to the interrogating

system through an isolator. The interrogating system consists of a fiber-optic interferometer as a wavelength discriminator and the following demodulation modules based on aforementioned passive homodyne interrogating scheme. To eliminate polarization induced signal fading, a Michelson interferometer is employed. It is formed by two ports of the $3 \times 3$ coupler as two paths of the interferometer and two faraday rotation mirrors (FRM) at the ends of both paths as reflectors. The imbalance between the two paths is $l = 20.55m$ by which the frequency change of the DFB fiber laser is converted to the intensity modulation and this conversion can be described by

$$\frac{\Delta\phi}{\Delta\nu} = \frac{4\pi nl}{c} = 1.23\ \mu rad/Hz \tag{2.25}$$

for $n = 1.468$ as effective refractive index of the optical fiber and $c = 3 \times 10^8\ m/s$ as the speed of light. The intensity-modulated light is then fed into the interrogating part of the configuration for phase demodulation on a computer (PC). Three amplified photodetectors (Optiphase V-600 of 2 and 1 Thorlabs PDA10CS) and a data acquisition card (DAQ card: NI USB-6251) are used to measure and digitize the three outputs of the $3\times3$ coupler respectively, one of which is routed through the circulator. Combining three outputs, the phase delay accumulated in the Michelson interferometer can be extracted. The respective output voltage $u(n)$ of the three photodetectors can be described as,

$$u(n) = R_F r(n) P(1 + V cos(\phi + n\frac{2}{3})\pi) \tag{2.26}$$

where $n = 1, 2, 3$ corresponding to the three photodetectors, $R_F$, r and P are for the feedback resistor in the detector's circuitry, photodiode responses (A/W) and the split optical power (W), V is the shared fringe visibility determined by the overall interferometer quality and $\phi$ is for the phase delay accumulated in the Michelson interferometer. The $\frac{2}{3}\pi$ phase shift

between three outputs are governed by the optical property of a true $3 \times 3$ coupler with equal power split ratio. The phase delay $\phi$ involve both strain induced phase and also the environmental noises. In the system calibration phase before tests, a strong phase modulation inside one arm of the interferometer is introduced by a built-in PZT such that the possible impact of difference of r and $R_F$ among three photodetectors can be removed. After the calibration, 2.26 is simplified to,

$$u_c(n) = 1 + Vcos(\phi + n\frac{2}{3})\pi \tag{2.27}$$

Based on 2.27, we can use the following two equations to calculate the $sin(\phi)$ and $\cos(\phi)$ simultaneously.

$$u_c(1)(cos(\frac{2\pi}{3}) - cos(\frac{-2\pi}{3})) + u_c(2)(cos(-\frac{2\pi}{3}) - 1) + u_c(3)(1 - cos(\frac{2\pi}{3})) = sin(\phi) \tag{2.28}$$

$$u_c(1)(sin(\frac{2\pi}{3}) - sin(\frac{-2\pi}{3})) + u_c(2)sin(-\frac{2\pi}{3}) - u_c(3)sin(\frac{2\pi}{3}) = cos(\phi) \tag{2.29}$$

It is clearly seen that with the three $\frac{2\pi}{3}$ phase shifted outputs from the $3 \times 3$ coupler, the phase delay in the interferometer can be always tracked in the range of $0 \sim 2\pi$ dynamically without using any kinds of feedback loops, which in our case corresponds to any strain induced phase change along the optical fiber. Phase unwrapping is further applied in the data processing to reveal large ($> 2\pi$) strain induced phase shift.

## 2.5 ALL-OPTICAL HOT-WIRE FLOW SENSOR

Gas flow measurement plays important roles in various industrial sectors. It provides vital information for a large number of applications such as process controls, fossil-fuel and nuclear electric power generation, transportation, environment monitoring and etc. To perform flow measurements, a large number of flow sensors based on various mechanical, electronic, and micro-electro-mechanical system (MEMS) structures [45] have been developed. These sensors can perform effective flow measurements at the room temperature or slightly elevated temperatures (e.g. $< 200\,^{\circ}\mathrm{C}$). However, a number of industrial and aerospace applications demand flow sensors with much higher operational temperatures ($> 500\,^{\circ}\mathrm{C}$). These are not attainable by current state of the arts such as MEMS technology. To address this technical challenge, a low-cost and compact all-optical-fiber flow sensing technique is presented which can provide rapid and accurate gas flow measurements from the room temperature to $800\,^{\circ}\mathrm{C}$. This is, to our best knowledge, the highest operational temperature for a flow sensor.

Fiber-optic sensors are well-known for their resilience in many harsh conditions including in high-temperature, corrosive, and strong electromagnetic environments. Over the last decade, various optical-fiber-based flow sensors have been reported, largely based on two schemes: fiber-optic interferometry [46–48] and optical hot-wire anemometry (Optical HWA). Among different designs of optical flow sensors, the HWA is one of the most widely adopted flow measurement techniques, thanks to its simplicity and reliability. The sensing elements of HWA-based flow sensors are electrically/optically heated with constant power in operation and determine flow rate by measuring heat transfer between a heated element and adjacent temperature sensors [49].

Compared with electrically heated HWA flow sensors, fiber-optic sensors can also be heated optically to perform flow measurements. Using various optical coupling schemes [50–55], in-fiber light has been used to heat up a section of fiber containing a sensing element (e.g. a fiber Bragg grating or FBG) to perform temperature measurements. The optical HWA can be more resilient than those using the electric heating for high-temperature applications. This is because the optical fiber, as a power delivery cable, can sustain much higher temperatures than metal wires.

In the later chapter of this thesis, we will demonstrate an all-optical hot-wire flow sensor capable of high-temperature flow measurements with compensations to ambient temperature changes. Using in-fiber light as both the heating power and the interrogation light source, a pair of high-temperature-stable RFBGs are used to gauge the heat transfer from an optically powered heating element (HAF) induced by the gas flow. The entire flow sensor is constructed in one silica fiber and interrogated/powered through one fiber feed through. Reliable gas flow measurements will be demonstrated for a wide temperature range from the room temperature to 800 °C. The fiber sensor technique can provides a low-cost and reliable solution for flow sensing for high-temperature harsh environments.

## 2.6 RAYLEIGH OPTICAL FREQUENCY DOMAIN REFLECTOMETER

### 2.6.1 Overview

Optical fibers have been developed and widely used as a medium for telecommunication and networking. In the same time, optical fiber based sensors offers several important advantages over conventional electronic sensors, including low manufacture cost, miniature and flexible structure, immunity to electromagnetic fields (IMFs), long lifetime, and the capability of sensing multiple parameters in harsh environments. The ultra-low transmission loss and huge optical bandwidth allow the deployment of real-time sensor network for remote and distributed sensing. The intensity, phase, polarization, wavelength or delay time of light in the fiber can all be interrogated to measure temperature, strain, pressure, ambient refractive index, displacement and other quantities. Extrinsic fiber sensors use optical fiber cables to transmit sensing signals from non-fiber traditional sensors. On the other hand, intrinsic fiber sensors, such as fiber Bragg gratings (FBG) and in-fiber Fabry-Perot interferometers (FPI), incorporate the functional transducer structure into the optical fiber, and minimize the transmission loss, device size, and energy consumption. For example, FBG sensors can be multiplexed either with different Bragg wavelengths or with the same Bragg wavelength but at different spatial positions and therefore time delays. Very high spatial resolution can be achieved due to the miniature size of a single FBG, but the distributed sensing capability is still limited by the number of gratings that can be multiplexed on a single optical fiber.

Fully distributed sensing was first demonstrated using in-fiber Brillouin scattering measurement with optical fiber itself treated as the sensing element [56]. In-fiber Brillouin scattering is spatially interrogated with meter-resolution using optical time domain reflec-

tometry (OTDR) technology, where distributed measurements are essentially based on the time of fly of sent laser pulses to reveal distance information. Therefore, the pulse duration and also the performance of the electronic photoreceivers which detect reflected laser pulses both limit the actual resolutions of the OTDR systems. Compared with OTDR, the optical frequency domain reflectometry (OFDR) sensing technique relinquishes the necessity of pulse lasers and high-speed electronics, and offers significantly higher spatial resolution. Recently, centimeter-resolution distributed sensing were reported using OFDR in-fiber Rayleigh scattering measurements [57, 58]. In this dissertation, we further employ this technique and transform it into a general 3D strain imaging technique in concrete structures. In the following section, the brief review of how this OFDR technique works will be covered.

### 2.6.2 System Composition and Sensing Mechanism

In-fiber Rayleigh scattering is based on elastic scattering of light in optical fibers. Due to the nature of fused silica and its manufacturing process, the optical fibers are pretty coarse on sub-wavelength scales such that density distribution along the optical fiber suffered from random variations, from where the in-fiber Rayleigh scattering is derived. Such randomly varied density distribution can be interrogated by OFDR method and with cross referencing between the Rayleigh scattering signatures of the original optical fiber and the same one under perturbation, the ambient perturbation can be quantified. The OFDR method based on in-fiber Rayleigh scatter can provide distributed strain and temperature sensing with centimeter resolution. However, without careful designs only one parameter can be retrieved at once since both perturbations exert the same effects embodied on backscattered Rayleigh signals.

The principle of in-fiber Rayleigh scattering measurement for distributed fiber sensing has been extensively reported [59–61]. It can be explained in brief using the OFDR diagram as illustrated in Fig. 12. The OFDR setup consists of the coherent tunable light source, the fiber interferometer, and the photodetectors. Light from a CW laser is linearly swept and coupled into a fiber interferometer at frequency,

$$\omega(t) = \omega_0 + \gamma t \tag{2.30}$$

where $\gamma$ is the wavelength tuning rate and $t$ is the laboratory time. The fiber interferometer is composed of measurement and reference arms. The measurement arm of the interferometer is connected to the fiber under test (FUT) using a fiber optic circulator. At the location $x$, Rayleigh scattering signal and possible discrete reflection signals excited by the probe light in the FUT are reflected back to the OFDR system through the fiber optic circulator and recombined with the reference arm light before the polarizing beamsplitter and the two

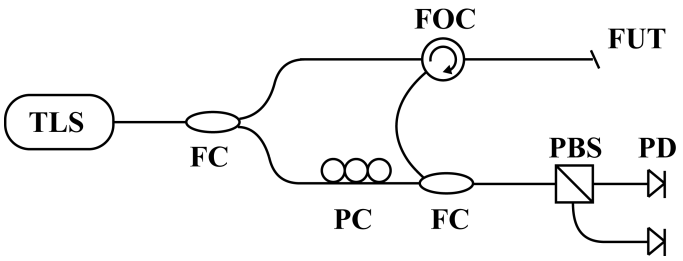


Figure 12: The schematic of in-fiber Rayleigh scattering measurement using OFDR. TLS: tunable laser source; FC: fiber coupler; PC: polarization controller; FOC: fiber optic circulator; PBS: polarizing beamsplitter; FUT: fiber under test; PD: photodetector.

photodetectors. When polarization effects are not considered, the electrical fields of the backscattering signal can be expressed as below,

$$E_{Rayleigh} = E_0(t+\tau_2) \cdot \rho(\omega) \cdot e^{-i\omega(t+\tau_2)+i\phi(\omega)} \tag{2.31}$$

$$E_{ref} = E_0(t+\tau_1) \cdot e^{-i\omega(t+\tau_1)} \tag{2.32}$$

where $\tau_2$ and $\tau_1$ are the time delay for measurement arm path at a location $x$ and the reference arm path respectively, $\rho(\omega)$ and $\phi(\omega)$ are the Rayleigh gain and phase shift. Upon recombination, the light intensity measured by the photodetectors are expressed as below with $\tau = \tau_2 - \tau_1$,

$$I(\omega) = |E_0(t)|^2 + |E(t-\tau) \cdot \rho(\omega)|^2 + 2E_0(t) \cdot E_0(t-\tau) \cdot \rho(\omega) cos[\omega\tau - \phi(\omega)] \tag{2.33}$$

in which the location information of the Rayleigh backscattering has been encoded into the oscillating terms on the right hand side. After the wavelength-swept measurement, such encoded location information can be retrieved through fast Fourier transform [59].

$$I(\tau) = I(n \cdot \Delta x/c) = FFT[I(\omega)] \tag{2.34}$$

where $n$ is the effective refractive index of the optical fiber under test, $c$ is equal to the speed of light, and $\Delta x$ corresponds to the optical path difference of location $x$ with respect to the reference arm path.

Therefore the Rayleigh scattering profile and possible discrete reflection information versus fiber length can be obtained. The maximum probing length is theoretically determined by the differential delay $\tau_d$ in an auxiliary interferometer which is in parallel to optic structure shown in Fig. 12 and intended to trigger digital data acquisition accurately with equal

frequency spacing during the scan, and the spatial resolution is determined by the wavelength sweeping range $\Delta f_{sweep}$ of the coherent light source, as is shown below

$$L_{max} = \frac{c\tau_d}{4n}, \Delta L = \frac{c}{2n\Delta f_{sweep}} \tag{2.35}$$

The two equations above are both obtained through general discrete sampling theorem so it is also worth noting that the actual maximum probing length is still fundamentally limited by the coherence length of the tunable laser.

As mentioned previously by cross-correlating with a pre-measured reference for a certain section of FUT, i.e. 1-cm-long section, in frequency domain, Rayleigh spectral shifts induced by external perturbations such as temperature or strain changes along the same section of the FUT can be interrogated [57, 62]. The temperature or strain changes are quantified by

$$\frac{\Delta\lambda}{\lambda} = -\frac{\Delta\nu}{\nu} = K_T\Delta T + K_\epsilon\Delta\epsilon \tag{2.36}$$

where $K_T$ is the thermal-optic coefficient and $K_\epsilon$ is the strain coefficient. Such cross-correlation procedure can be carried out over the whole FUT with the step size of 1-cm in length, by which the distributed measurements along the FUT is obtained.

# 3.0 REGENERATED DISTRIBUTED BRAGG REFLECTOR (RDBR) FIBER LASERS

## 3.1 OVERVIEW

In this work, we present studies and characterization of high-temperature stable distributed Bragg reflector (DBR) fiber lasers using the regenerative grating technique. The results described in this chapter have been published [63]. Two regenerated gratings are used as reflectors in a DBR fiber laser for high-temperature operation. The laser performance was characterized from the room temperature to 750 °C. Continuous monitoring for the laser output power was performed to quantify its stability at elevated temperatures. The regenerated gratings and output power of the laser are shown to be stable at 750 °C for more than 7 hours. For fiber lasers demanding high-temperature stability or high-power operation, regenerated grating based DBR fiber laser (RDBR) stands out as a simple and reliable solution.

## 3.2 FABRICATION METHODS

Regenerative gratings were fabricated in standard telecommunications fibers (Corning SMF-28) in this work. To enhance photosensitivity, the fibers were soaked in a hydrogen chamber at $T \sim 25\,^{\circ}\mathrm{C}$, $P \sim 2400psi(165bars)$ for about 1 week. Two $L = 2.5cm$ long FBGs with $\lambda_{Bragg} \sim 1550nm$ were inscribed into the fiber core using a 248 nm KrF laser and a phase mask. A cumulative fluence of $f_{cum} = 1.32kJ/cm^2$ was used to produce highly saturated gratings at $\sim 50mJ/cm^2$ radiation intensity. The spectra of two seed gratings with matched resonant wavelengths are shown in Fig. 13. Excessive UV exposures induced $\Delta n_{DC} > 10^{-3}$ index change in the fiber core and index modulations were estimated to be $\Delta n_1 = 0.0015$ and $\Delta n_2 = 0.0013$ for the two gratings FBG1 and FBG2 respectively shown in Fig. 13

Two matched gratings were fusion spliced to both ends of a 15 cm long erbium doped fiber with absorption of 57.0 dB/m at 980 nm (ER110-4/125 by nLight). The FBG2 in Fig. 13 with relatively weaker index modulation was used as the output coupler for the laser cavity. The spliced fiber was then post-hydrogen-loaded [22] in the hydrogen chamber for $t =\sim 2$ days before the regeneration process. After being removed from the hydrogen chamber, the fiber laser was immediately taken to a box furnace for thermal treatment. The temperature of the furnace was isochronally raised up to $T = 800\,^{\circ}\mathrm{C}$ in $t \sim 2.5hr$. Seed gratings were then annealed at $T = 800\,^{\circ}\mathrm{C}$ for $t > 50hr$. The evolution of the grating spectrum is shown in Fig. 14, and the changes for Bragg and reflection are shown in Fig. 15. It is worth noting that the regeneration process of the two gratings was measured together. Thus both of the gratings contributed to the reflection and the curve of peak wavelength shown in Fig. 15. There are five steps involved in the regeneration process. During Step

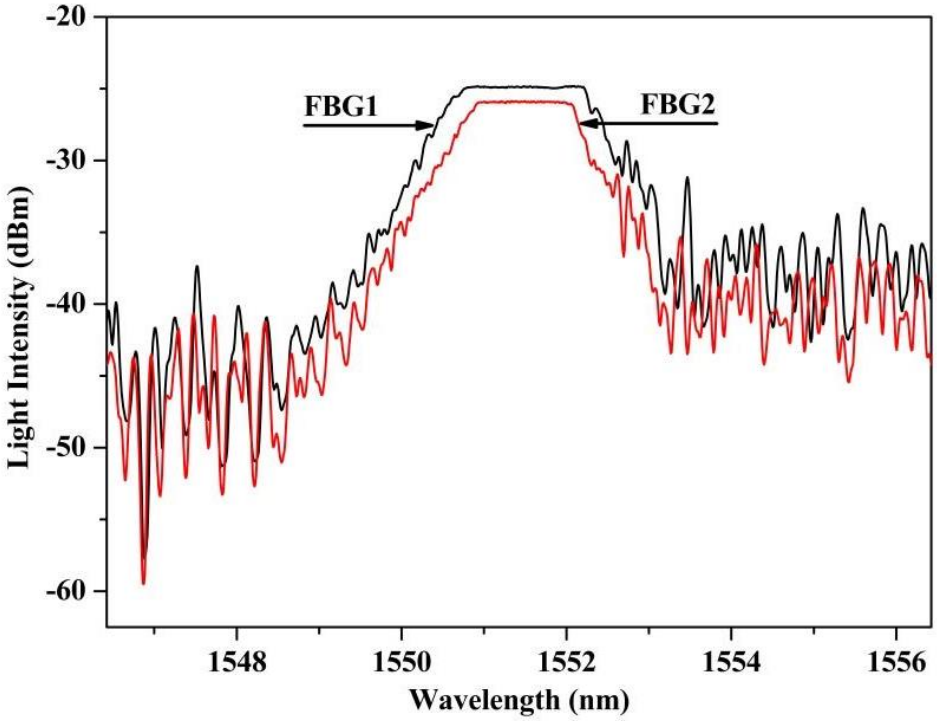


Figure 13: Reflection spectra of the two matched fiber Bragg gratings.

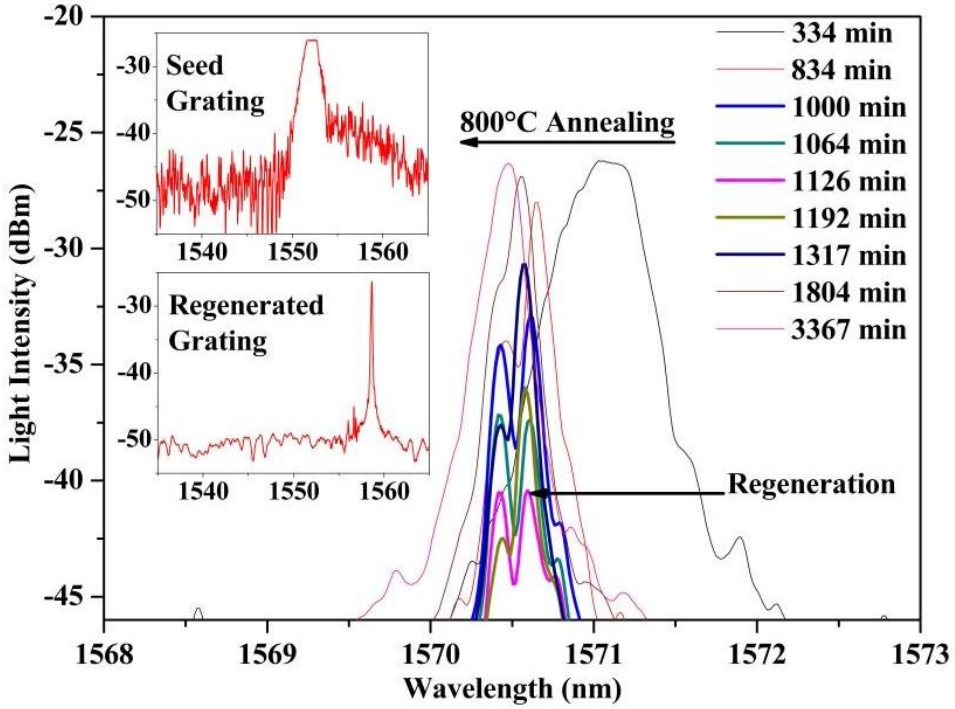


Figure 14: Evolution of grating reflection spectra. Insets, reflection spectra of the seed at room temperature ($T = 26\,^{\circ}\mathrm{C}$) and regenerated grating at $800\,^{\circ}\mathrm{C}$.

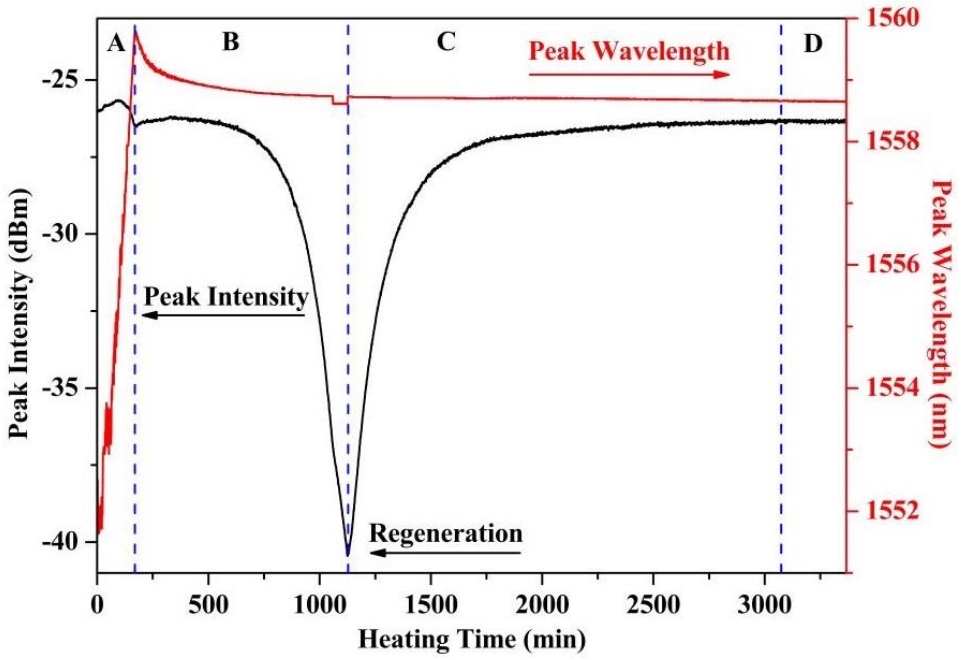


Figure 15: Changes of grating strength and resonate wavelength during the regeneration process.

A labeled in Fig. 15, the temperature of the box furnace isochronally increased at the rate of $5\,^{\circ}\mathrm{C}/min$. A slow growth in reflection was initially observed. This is mainly due to the degraded absorption of erbium doped fiber [64]. When the fiber temperature was raised to $T = 800\,^{\circ}\mathrm{C}$, the isothermal annealing started. The erasure of the seed gratings occurred during this period (labeled as Step B). This was followed by grating regeneration labeled as Step C. The strength of the regenerated gratings increased steadily during this period. A blue shift in $\lambda_{Bragg}$ was also observed in Step B and C, which is attributed to relaxation of UV-induced $\Delta n_{DC}$. At the early stage of the regeneration, double reflection peaks were on site as shown in Fig. 14 . It is probably derived from the slightly different regeneration paces of FBG1 and FBG2, respectively. Peak reflectivity of regenerated FBGs increased and became stabilized after $t \sim 32hr$. The double-peak features disappeared once both FBGs were stabilized. In the last step, the regenerated FBGs were allowed to stabilize for another 5 hours till the FBG wavelength fluctuation was below the minimal resolution of the optical spectrum analyzer (OSA, Agilent 86140B with 70 pm resolution) and the fluctuation of FBG strength was also less than 0.01 dB/hr at $T = 800\,^{\circ}\mathrm{C}$. The index modulation of the regenerated grating FBG2 in Fig. 13 was estimated to be $\Delta n_{reg} = 0.36 \times 10^{-4}$, resulting in more than 10 dB rejection in transmission with a FWHM bandwidth of 130 pm.

## 3.3 FIBER LASER CHARACTERIZATION

After the thermal regeneration process, the lasing characterization of the fiber laser was performed in a box furnace. A 980 nm diode laser, a wavelength division multiplexer, and the OSA were used for optical pumping and measurements respectively. The laser performance

was characterized between room temperature ($T = 26\,^{\circ}\mathrm{C}$) and 750 °C, which is 50 °C below the regeneration temperature. Fig. 16 presents lasing wavelength dependence on temperatures. A linear wavelength-temperature coefficient $\frac{\partial\lambda}{\partial T} \sim 0.0137 nm/\,^{\circ}\mathrm{C}$ was obtained over the lasing wavelength tuning range for almost 10 nm between the room temperature and 750 °C.

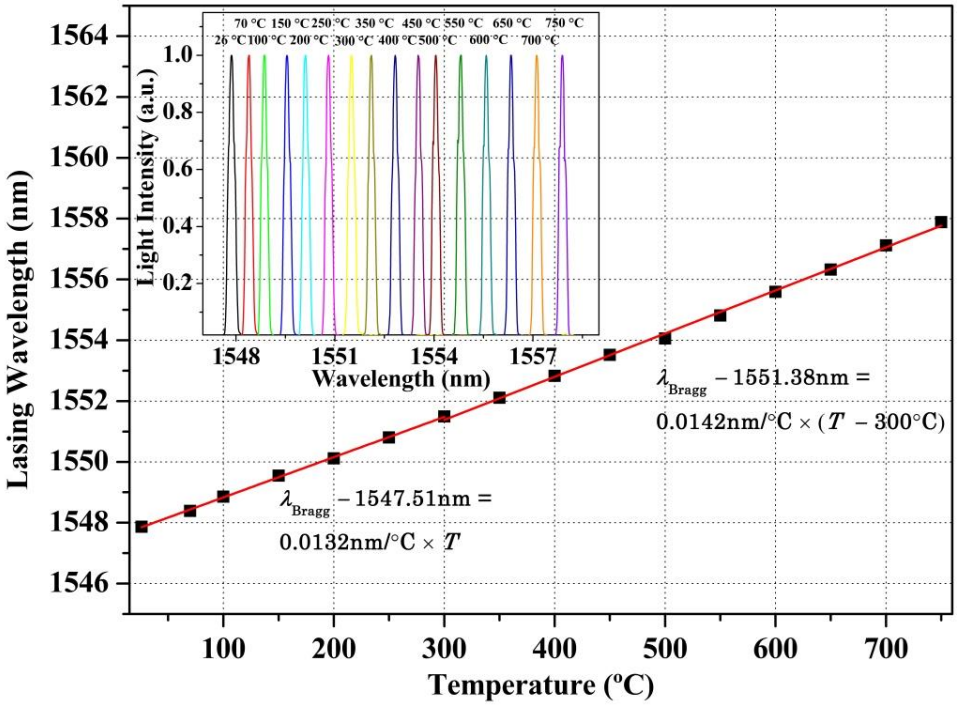


Figure 16: Wavelength shift of the fiber laser output. Inset, the normalized laser spectra under different temperatures.

The laser dynamics was further studied by quantifying the slope efficiency under different temperatures. Measurements of laser output versus pump power curves are shown in Fig. 17. At room temperature $T = 26\,^{\circ}\mathrm{C}$, the laser exhibits the slope efficiency of $\eta_s = 0.46\%$. When the temperature was raised to $T = 500\,^{\circ}\mathrm{C}$, the efficiency decreased to $\eta_s = 0.175\%$, due to the degraded gain spectrum, where the gain is depleted with increasing temperature by changing the saturated population inversion [64]. At the highest temperature $T = 750\,^{\circ}\mathrm{C}$,

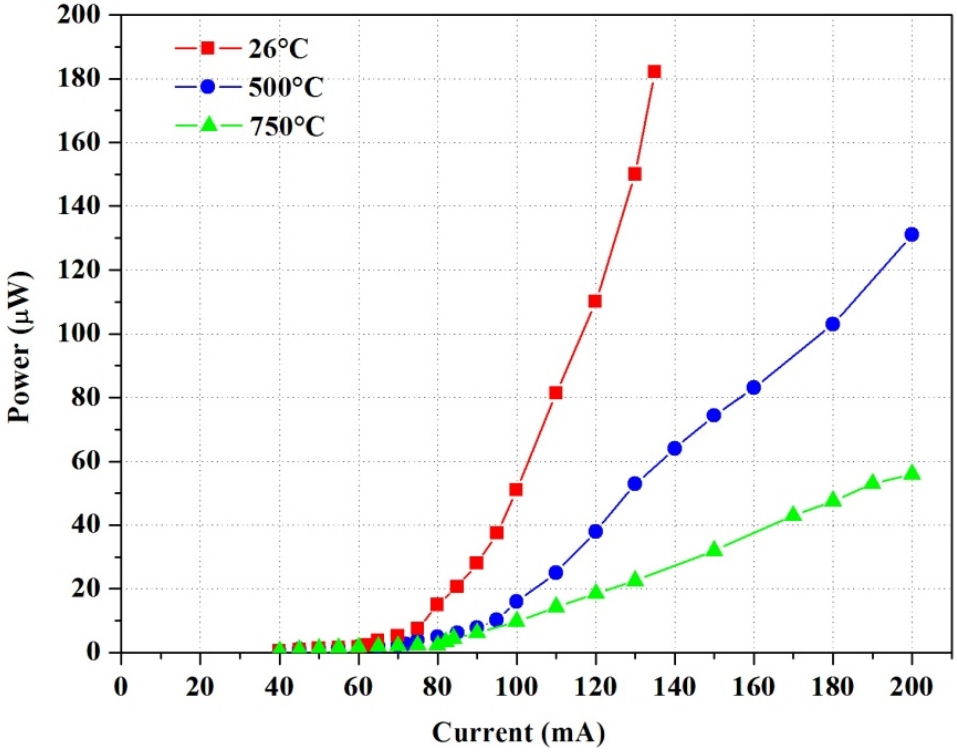


Figure 17: Fiber laser output versus 980 nm pump power at three different temperatures.

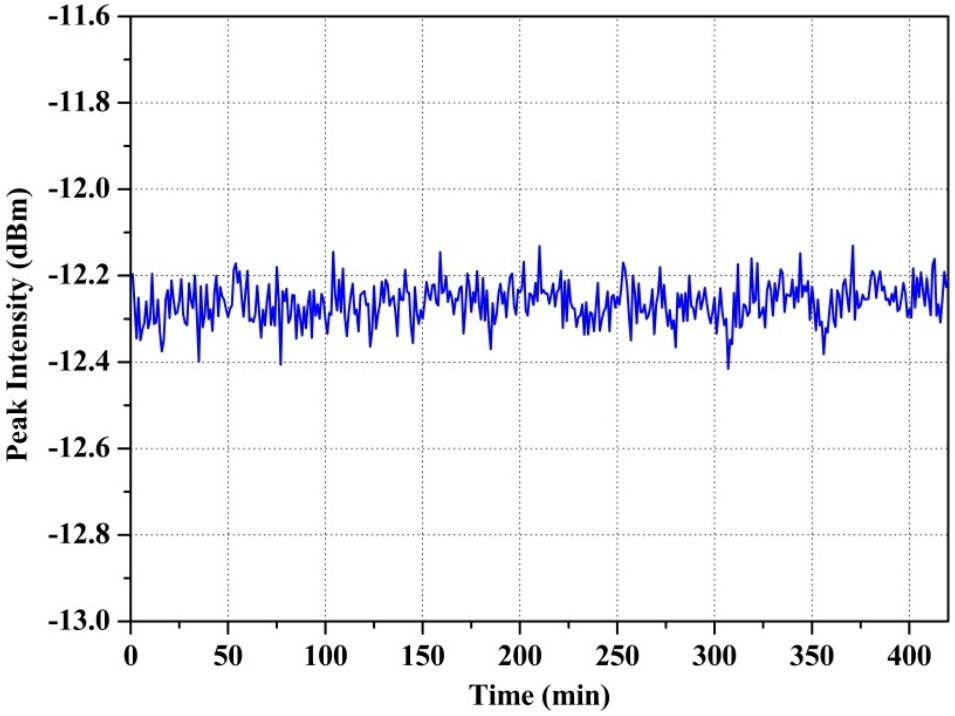


Figure 18: Measured fiber laser output power over 7 hours at 750 °C.

the laser efficiency was significantly reduced to $\eta_s = 0.069\%$. The lasing threshold also increases due to the gain degradation at high temperature. The threshold increased from $P_{th} = 20.264mW$ at the room temperature $T = 26\,^{\circ}\mathrm{C}$ to $P_{th} = 27.132mW$ at $T = 500\,^{\circ}\mathrm{C}$ and finally $P_{th} = 34.068mW$ at $T = 750\,^{\circ}\mathrm{C}$. Despite the gain degradation, the output power of the laser can reach $P_{out} > 1mW$ at all test temperatures.

To study high-temperature performance and stability of the fiber laser, several heating and cooling cycles between $26\,^{\circ}\mathrm{C}$ and $750\,^{\circ}\mathrm{C}$ was carried out for a period over 120 hr. No decay was observed in the grating strength nor the lasing characteristics. Fig. 18 shows the stability characteristics of laser output power during a period of 7 hours isothermal heating at $T = 750\,^{\circ}\mathrm{C}$. The optical pump for the fiber laser was set at $P_{pump} = 66.64mW$. The OSA was used to measure the fiber laser output every minute. The total output power fluctuation shown in Fig. 18 is 1.06% with a $60\mu W$ output power.

In summary, we have applied fiber grating thermal regeneration process, a low-cost and convenient treatment, to produce an erbium-doped DBR (or RDBR) fiber laser capable of long-term and stable operation up to $750\,^{\circ}\mathrm{C}$, possibly higher, despite the reduced gain at high temperatures, opening a new class of lasers designed for extreme environments. The resultant fiber laser endured several cycles of heating and cooling over the duration of $t > 120hr$, with no performance degradation observed, indicating strong high-temperature resistance and stability.

# 4.0 FIBER-OPTICS FLOW SENSORS FOR HIGH-TEMPERATURE OPERATION

## 4.1 OVERVIEW

In this chapter, we demonstrate an all-fiber high-temperature flow sensor using the optical HWA rated for 800 °C operation. This chapter details the results that have been published in [65]. The sensor consists of an in-fiber optical heating element using high-attenuation fibers (HAFs). High-temperature-stable regenerated FBGs (RFBG) [19–21] were induced in HAFs and standard telecom fibers (SMF-28) as temperature sensors to gauge flow-induced heat transfers. The schematic of the experiment setup is shown in Fig. 19. A high-power erbium doped fiber amplifier (EDFA) was built to provide up to 700-mW optical power to heat the HAF via a circulator. A RFBG in HAF was used to measure the temperature of the optical heating elements. Another RFBG formed in SMF-28 located at upper stream of the gas flow was used to measure the ambient temperature surrounding the heating element.

The wavelengths of FBG sensors were monitored by an optical spectrum analyzer (OSA, Agilent 86140B with 70 pm resolution). A tube furnace was used to provide high-temperature environments for sensor testing. During measurements, the fiber sensor was inserted in a quartz tube (OD: 6 mm, ID: 4 mm). At the input side, $N_2$ gas was introduced through a

tee tube fitting. The fiber was sealed using a rubber ferrule. At the exit of the flow tube, the fiber was placed on a tapered v-groove fiber holder (Thorlab HFV002) to ensure that no contact between the fiber and inner wall of the tube was made. A calibrated mass flow controller regulated the input flow rate of $N_2$ gas. The sensor was tested under flow rates from 50 cubic centimeters (CCM) to 500 CCM, corresponding to mean flow velocity at the entry of the quartz tube ranging from 0.066 m/s to 0.66 m/s. At this velocity range, the gas flow inside the quartz tube is considered as laminar only [66].

## 4.2 SENSOR FABRICATION

Unlike conventional Type I FBGs which normally degrade rapidly at temperatures, RFBGs can be stable at the same temperature where it is regenerated (800 °C to 1295 °C [21] ). This technique provides a low-cost approach to fabricate various sensors capable of high-temperature operations. To fabricate the fiber sensor based on regenerated gratings, two

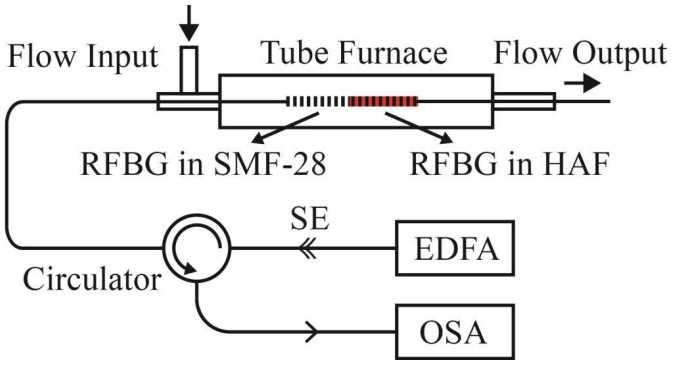


Figure 19: Schematic of the experiment setup for sensor calibration and characterization.

$L = 1cm$ long seed FBGs with $\lambda_{Bragg} \sim 1543.55nm$ and $\lambda_{Bragg} \sim 1546.75nm$ were inscribed in SMF-28 and HAF (CoreActive, attenuation coefficient 1 dB/cm) respectively. To enhance their photosensitivity, both optical fibers were soaked in a hydrogen chamber at $T \sim 25C$, $P \sim 2400psi(165bars)$ for about 1 week before the laser inscription. A 248-nm KrF excimer laser with pulse fluence $f_{pulse} \sim 50mJ/cm^2$ and repetition rate $RR = 20$ Hz was used to inscribe the FBGs. A cumulative fluence of $f_{cum} = 0.09kJ/cm^2$ was assigned to produce the FBG in SMF-28 while $f_{cum} = 1.2kJ/cm^2$ was applied to HAF. These lead to the FBG spectra shown in the left inset of Fig. 20. After the inscription, the samples were annealed at 120 °C for $t \sim 12$ hours. These two FBGs were then fusion spliced together to form the optical flow sensor as demonstrated as well in Fig. 19.

The regeneration process starts from a post-hydrogenation process [22]. Fiber sensor samples were first put back into the hydrogen chamber for post-hydrogen-loading at 2400 psi to enhance its photosensitivity. This is a key process for successful regeneration, especially for FBGs in HAFs. The post-hydrogen-loading lasted for $t = 1$ week. Then the fiber sample was placed in a box furnace for the thermal regeneration. A typical regeneration process is shown in Fig. 20. The temperature of the furnace was isochronally increased to 850 °C with a rate of 5 °C/$min$ in step A and then held steady in both step B and C for isothermal annealing. FBGs in both SMF-28 and HAF were annealed rapidly as the temperature rose (step A), however, with different decay patterns. This is probably due to double-cladding fiber structures in HAF. During the grating erasure, the onset of a blue shift in $\lambda_{Bragg}$ is attributed to the thermal relaxation of UV-induced average refraction index change $\Delta n_{DC}$. The full erasure of both FBGs occurred at the end of step B, which lasted $t \sim 250$ min. This was followed by their subsequent grating regeneration in step C. Fig. 20 shows that

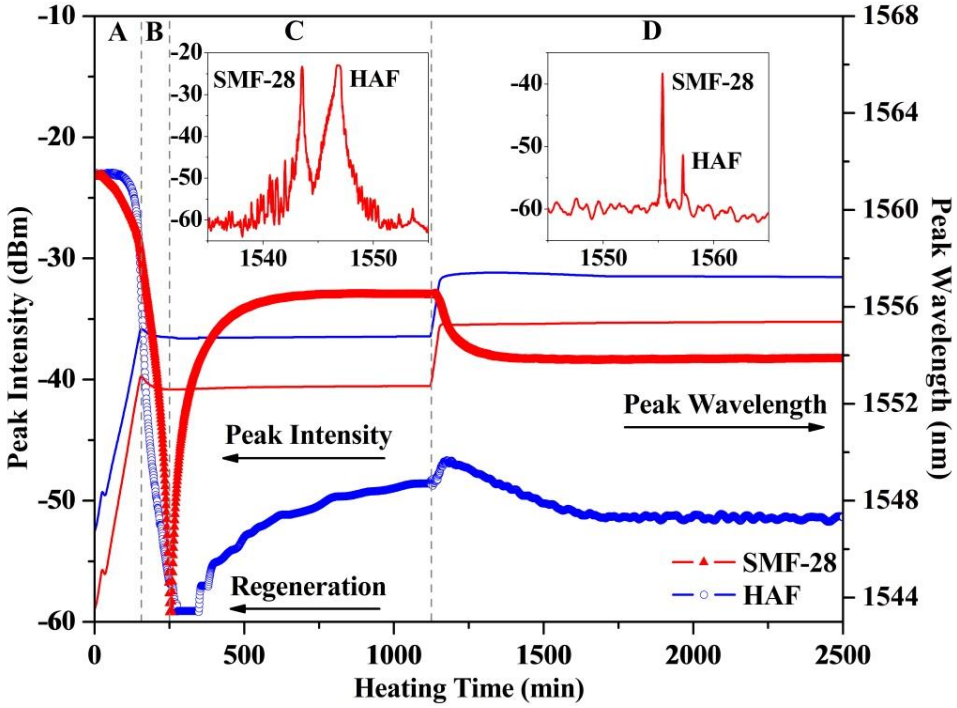


Figure 20: Changes of grating strengths and resonant wavelengths during the regeneration process for FBG in SMF-28 (red) and HAF (blue) respectively. The dot traces are for FBG peak intensity while line traces are for FBG wavelength. Insets, reflection spectra of the seeds at room temperature ($T = 25\,^{\circ}\mathrm{C}$) and regenerated gratings at $1000\,^{\circ}\mathrm{C}$.

the FBG in SMF-28 was regenerated much faster than that in HAF. When both RFBGs approached their steady states after $t \sim 870$ min of the thermal annealing at $T = 850\,^{\circ}\mathrm{C}$, the furnace temperature was elevated to 1000 °C for RFBG stabilization with the same rate of $5\,^{\circ}\mathrm{C}/min$ as shown in step D. Both FBGs were finally stabilized after $t \sim 580min$ of isothermal annealing at 1000 °C.

Once FBGs were regenerated, the flow sensor was characterized using the experiment setup shown in Fig. 19. The thermal responses of the two gratings were first measured and presented in Fig. 21. RFBGs in both HAF and SMF-28 exhibit slightly different thermo-optic coefficients for temperature from the room temperature to 300 °C and from 300 °C to 800 °C [64] where piecewise linear regression was used to evaluate the wavelength-temperature coefficients $\partial\lambda/\partial T$ of FBGs in two temperature ranges as shown in Fig. 21. The wavelength-temperature coefficients determined in Fig. 21 are important to gauge optical heating performance of HAFs.

## 4.3 FLOW METER CHARACTERIZATION

The optical heating of the HAF sensor under different ambient temperatures was quantified by injecting optical power from the EDFA from 0 to 700 mW. Not all optical power was absorbed by the HAF. It was estimated that the optical power absorbed by the 1-cm HAF was 14 mW/mm with 700-mW input power. The optical heating performance of the HAF from the room temperature to 800 °C is presented in Fig. 22. The largest shift of resonant wavelength for the RFBG in HAF is equal to $\Delta\lambda = 2.31nm$, corresponding to $\Delta T = 197.44\,^{\circ}\mathrm{C}$ at the room temperature. As ambient temperature increases, the optical heating becomes

less efficient. At 800 °C the shift of resonant wavelength was reduced to $\Delta\lambda = 1.09nm$ using 700-mW optical power, corresponding to $\Delta = 73.65\,°C$.

The operations of the flow sensor at the room temperature and at 800 °C are shown in Fig. 23. Reflection spectra for RFBGs in SMF-28 and HAF in ambient temperatures are shown in black traces. When the HAF section of the fiber absorbed optical power of 14 mW/mm at the room temperature (Fig. 23a), the RFBG wavelength in the HAF shifted for $\Delta\lambda_3 = 2.31nm$ ($\Delta T = 197.44\,°C$). The upper stream RFBG in SMF-28 also experienced a small red shift in resonant wavelength for $\Delta\lambda_1 = 0.13nm$, equivalent to temperature rise $\Delta \sim 11\,°C$ as shown in Fig. 23a, which was majorly due to the thermal conduction between two grating areas. The temperature of this upper stream RFBG sensor would be used as the reference to gauge the ambient temperature surrounding the heated element (HAF). Thereafter, the flow of $N_2$ was applied with a rate of 500 CCM (0.66 m/s), where

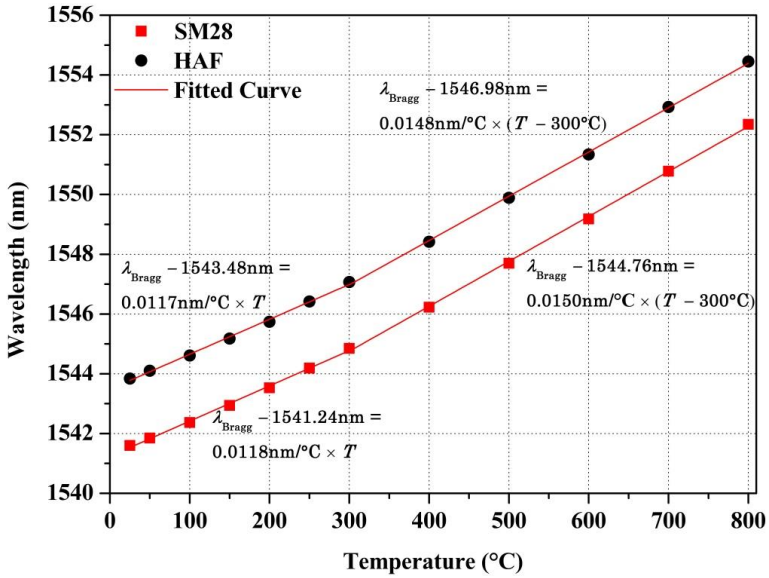


Figure 21: Resonance wavelength versus ambient temperature for both RFBGs.

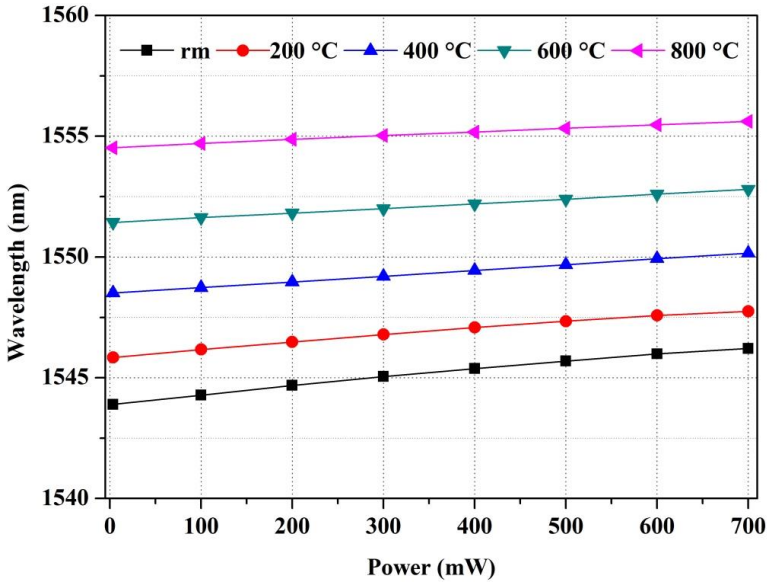


Figure 22: Heating performance of the HAF under different ambient temperatures.

convection cooling becomes the major factor responsible for heat loss of the HAF. The resonant wavelength of the upper stream RFBG in SMF-28 shifted back toward its original by $\Delta\lambda_2 = 0.15nm$, lowering the surface temperature of the sensor to $T = 23.31\,^{\circ}\mathrm{C}$ which was nearly $2\,^{\circ}\mathrm{C}$ lower than the preset ambient temperature $T = 25\,^{\circ}\mathrm{C}$, probably due to the temperature drop of decompressed $N_2$ itself. Meanwhile, the RFBG of HAF incurred a great blue shift in resonant wavelength for $\Delta\lambda_4 = -0.71nm$, corresponding to a temperature drop for $\Delta = 60.68\,^{\circ}\mathrm{C}$.

At $T = 800\,^{\circ}\mathrm{C}$, the absorption of 14 mW/mm optical power produced smaller wavelength shifts for both the reference RFBG ($\Delta\lambda_1 = 0.06nm$) and the RFBG in HAF ($\Delta\lambda_3 = 1.09nm$) as shown in Fig. 23b. The introduction of 500-CCM $N_2$ gas flow shifted the wavelength of the reference RFBG back to its original position ($\Delta\lambda_2 = -0.06nm$). A blue shift $\Delta\lambda_4 = -0.15nm$ of the RFBG wavelength in HAF was observed, corresponding to a temperature

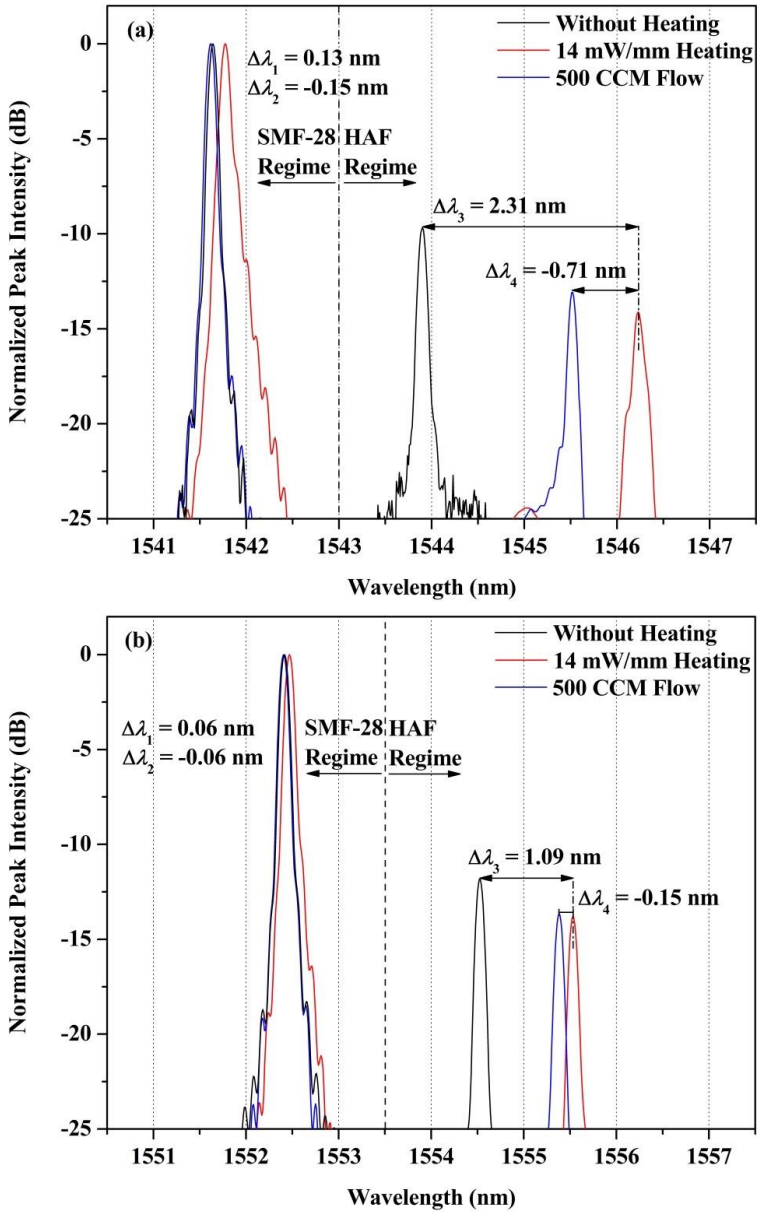


Figure 23: Reflection spectra of both RFBGs in SMF-28 and HAF under different heating, flow conditions and ambient temperatures: (a) 25 °C; (b) 800 °C.

drop $\Delta = -10.14\,^{\circ}\mathrm{C}$ of the optically heated HAF. The temperature drops measured by the RFBG in HAF and the reference temperature measured by the RFBG in SMF-28 can be combined to gauge the flow rate of $N_2$.

For a HWA flow sensor, the temperature change from the heating element due to the gas flow can be related to the flow velocity $\nu$ by [49],

$$H_{power} = \Delta T_h(A + B\sqrt{\nu}) \tag{4.1}$$

where $H_{power}$ is the power absorbed by the heating element, $\Delta_h$ is the temperature change from the ambient background on the HWA induced by an isothermal flow field, A and B are empirical coefficients. In our case, $\Delta_h$ is determined by the temperature changes on the heated RFBG in HAF and the ambient temperature measured by the reference RFBG in SMF-28 located at the upper stream of the gas flow according to,

$$\Delta T_h = (\frac{\partial \lambda}{\partial T})^{-1}_{HAF}(\Delta\lambda_3 + \Delta\lambda_4) + (\frac{\partial \lambda}{\partial T})^{-1}_{SMF-28}(\Delta\lambda_1 + \Delta\lambda_2) \tag{4.2}$$

where $(\partial\lambda/dT)_{HAF}$ and $(\partial\lambda/dT)_{SMF-28}$ are the wavelength-temperature coefficients of RFBGs in both HAF and SMF-28 fibers, which are determined by Fig. 21. The accurate measurement of the ambient temperature by the reference RFBG is critical to ensure accurate flow measurements. This is because that the introduction of gas flow can alter the ambient temperature in the vicinity of the HWA sensors [67].

The performance of the flow sensor under the maximum optical heating power (14 mW/mm) was quantified and shown in Fig. 24 with fitted curves derived from (4.1). The empirical coefficients A and B of every fitted curve are also included in the figure. The fitted curves match well with the experimental flow measurements at all temperatures. This indicates effective operation of the all-fiber hot-wire flow sensor operating under both the room

temperature and at elevated temperatures. Due to the nature of HWA, the sensitivity of the sensor reduces at high temperatures due to lower heating efficiencies of the HAF. However, this problem can be remedied by increased optical heating power or using HAF with higher attenuation coefficients.

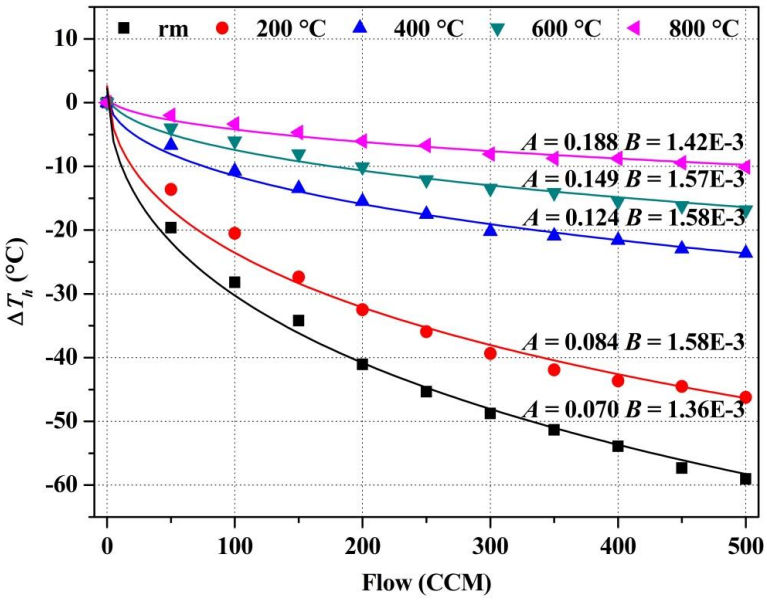


Figure 24: Calibrated sensor responses of the flow under different ambient temperatures shown with fitted curves based on the HWA theory.

# 5.0 USING DFB FIBER LASER TO MONITOR ACOUSTIC SIGNALS IN HYDRAULIC FRACTURING

## 5.1 OVERVIEW

Hydraulic fracturing is a widespread and often critical component in the development of oil and gas wells. It has been used extensively for over 60 years and growth in the technology has played a major role in opening new oil and gas resources in the US and overseas [68]. Therefore, it is important to study the mechanical process of hydraulic fracture growth in order to develop more efficient and sustainable fracturing schemes.

An important approach to studying the dynamics of hydraulic fracturing entails monitoring acoustic emission (AE) during the hydraulic fracturing process. Careful studies of AE signatures provide information on the location, distribution, size, and growth of fractures which can in turn be used to optimize the fracturing processes. Piezo-electric (PZT) acoustic sensors have been utilized extensively to study fracturing events with many successes [69,70]. However, when PZT acoustic sensors are implemented to monitor fracturing over large size samples or for downhole applications it can be challenging due to the lack of multiplexing capability and susceptibility of the sensors to harsh environments and electromagnetic interference. In the light of these difficulties of PZT-based sensors, this paper explores the

feasibility to utilize the ultra-high sensitivity of distributed feedback (DFB) fiber laser strain sensors [38] to monitor hydraulic fracturing process. As a fiber-based sensing scheme, DFB acoustic sensors are highly sensitive to acoustic emission. They can also be multiplexed in one fiber cable, and they are immune to complex electromagnetic environments in downhole scenario. Part of the results discussed in this chapter have been published in [71].

DFB fiber lasers used in this work were fabricated with a CW frequency-doubled argon-ion laser at 244 nm. The DFB fiber laser sensor used for the AE detection is composed of a section of 45-mm-long uniform phase-shift FBG inscribed on photosensitive erbium doped fiber [36]. The DFB fiber laser was pumped by a 980-nm diode laser with a pumping threshold of ∼1 mW. During the acoustic measurements, the output power of the DFB fiber laser was maintained at 80 $\mu W$ with a single longitudinal mode output. A fully passive homodyne interrogating scheme based on a $3 \times 3$ fiber coupler was used to interrogate DFB fiber laser sensor [42].

## 5.2 SENSOR MOUNTING CONFIGURATIONS

To our knowledge, no analogous measurements has been taken before to characterize DFB fiber laser strain sensors in measuring acoustic signals propagating through the solid materials and neither do its corresponding sensor mounting configurations. However, in order to optimize the fiber laser sensor performance, a proper mounting configuration is essential to fit the application. In this section, two sensor mounting configurations, as shown in Fig. 25a and c, were studied at first in order to determine the most sensitive solution for acoustic emission (AE) detection in solid materials with pencil lead break tests. In the figure, we see

two DFB fiber lasers were attached to corresponding mounting materials. Polyamide film tapes were used to attach the optical fiber. Besides, thermal paste was also applied over the cavity region of the fiber laser to enhance the contact. For mounting of DFB fiber laser strain sensors, a typical configuration, the tube or mandrel based configuration, often used with hydrophones was chosen at the first place considering its well known characteristics as acoustic amplifier [72]. In this work, the mandrel is made out of polycarbonate, aiming at preserve the non-conductivity optical fibers. Although the mandrel configuration has been proved successful in development of hydrophones, its application can still be limited by its bulky sizes, preventing it from being placed close to the potential AE sources. Therefore, another mounting configuration with much smaller size was proposed: the polycarbonate bar configuration.

To verify the practical application of both mounting configurations, AE tests were carried out on a 61 cm $\times$ 41 cm $\times$ 1.8 mm aluminium plate with 0.5-mm diameter pencil leads. The standard test procedure entailing 3-mm lead length and 30 $^\circ$ contact angle was followed to ensure consistent measurements. The AE were generated at the centre of the plate by breaking the pencil leads. The generated acoustic waves propagated toward and were received by the DFB fiber laser sensor. During the test, the distance between the AE source and the centre of the laser cavity (bar) or the geometrical centre of the polycarbonate mandrel (mandrel) was maintained to be 15 cm. Ultrasonic gel (mixed propylene glycol, glycerine and water) was used to enhance the transduction of sound energy from the aluminium plate to the DFB laser sensors. The mounted sensors were positioned in three different locations with respect to the AE source, with intention to characterize the directionality of sensing performance for both mounting configurations.

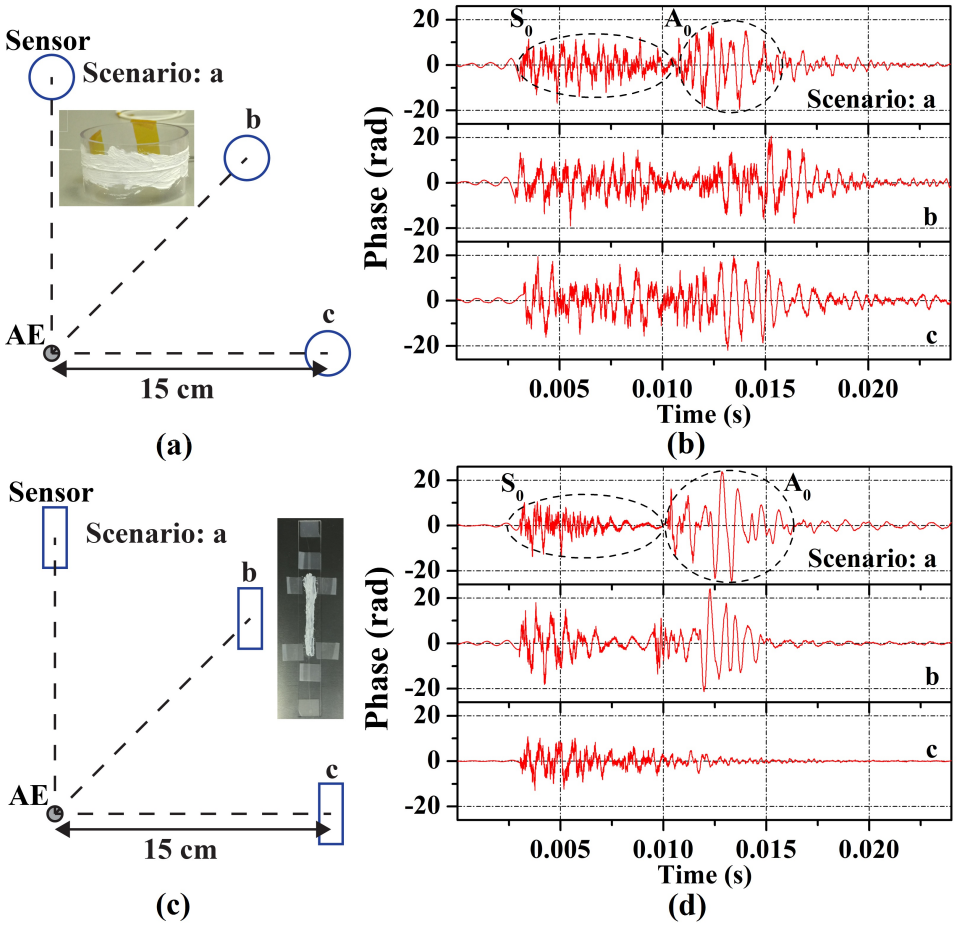


Figure 25: Proposed DFB fiber laser mounting configurations: (a) Schematic of the tube-mounting sensor position relative to the AE source; Inset: Photo of a 5-cm diameter polycarbonate tube with 3-mm wall thickness and 2.54-cm height with the fiber laser mounted; (b) Pencil-lead break test results for the tube mounting configuration; (c) Schematic of the bar-mounting sensor position relative to the AE source; Inset: Photo of a 22 cm × 2.54 cm × 2.4 mm polycarbonate bar mounted with the fiber laser and attached to the aluminium plate; (d) Pencil-lead break test results for the bar mounting configuration.

The experiment results are shown in Fig. 25b and d. Output data is the unwrapped optical phase delay detected by the interferometer used in the interrogation system. The phase change ($\Delta\phi$) at any given point of time is linearly related to the local strain change ($\Delta\epsilon$) applied on the DFB fiber laser according to $\Delta\phi/\Delta\epsilon = 1.91 \times 10^8 rad/\epsilon$ (20.55-m imbalance path used in the interrogation system) [38]. A 1-KHz high pass filter was used to remove low-frequency environmental noises and to reveal high-frequency lamb wave components [73]. Using the mandrel configuration, both symmetrical $S_0$ and asymmetrical $A_0$ modes of the Lamb wave are observed with good signal to noise ratio as shown in Fig. 25b. In this mounting configuration, the DFB laser sensors sensitivity is independent to the direction of AE. Measurements performed by the DFB laser with the bar configuration are shown in Fig. 25d. The sensitivity of the mounted sensor deceases as approaching direction of acoustic waves deviate from the axial direction of the fiber laser cavity. This is revealed in Fig. 25d where $A_0$ components are highly sensitive to the relative orientation of the DFB laser cavity and the propagation direction of AE waves.

## 5.3 MONITORING OF HYDRAULIC FRACTURING PROCESS

After verifying the suitable mounting configurations, the DFB fiber laser strain sensor mounted on the polycarbonate mandrel was used to monitor hydraulic fracturing induced on a $15 \times 15 \times 15\ cm^3$ granite block. The mounted sensor was attached on a surface of the block with the same ultrasonic gel, as shown in Fig. 26. The hydraulic fracturing was induced by injecting 2500-psi propellant (glycerin) through and released by the tubing at the centre of the block through a pair of perforations, where initial fracturing was induced.

The onset of major breakdown occurred after 400 seconds of pressurization. The strain measurements by the DFB laser, which was converted from the optical phase measured by the passive homodyne interrogator, are shown in Fig. 26. Two acoustic emission features were evident. One is the high frequency AE signals associated with cracking process. Their frequency components are generally over 10 KHz with $< 50$ $n\epsilon$ in amplitude and can be separated out from the original measurement by using a 10-KHz high pass filter as shown in Fig. 27. The other feature is the AE signals with lower frequency. They are large in quantity ($> 12$ $\mu\epsilon$) of static strain. This feature is due to the static change in strain applied to the fiber laser due to the enlargement of the rock as the cracks formed. They are also responsible for the permanent strain change left on the fiber laser after the major fracturing. The specimen could not contract after the fracturing, which inevitably left static strain on the fiber laser via a loose bonding (ultrasonic gel) between the sensor-mounted mandrel and the specimen. The curve of hydraulic pressure applied inside the tubing is also presented in the Fig. 26 for comparison. The time of sudden release of the hydraulic pressure matches well with the time when strong strain changes are observed, confirming the measurement results from the DFB sensor are derived from the fracturing process.

Another useful analysis in the area of hydraulic fracturing research is to extract and study AE counts, where the obtained data can be correlated with the evolution of structural failure [70]. In our test, cumulative count for the AE is defined as number of amplitude threshold crossings of the 10-KHz high pass filtered strain measurement. The plot for the cumulative AE count versus time is presented in Fig. 28. The counting was conducted based on a threshold set to 0.5 $n\epsilon$. The value is determined to efficiently remove environmental noises but is able to distinguish AE signals of cracks induced by the hydraulic pressure. As

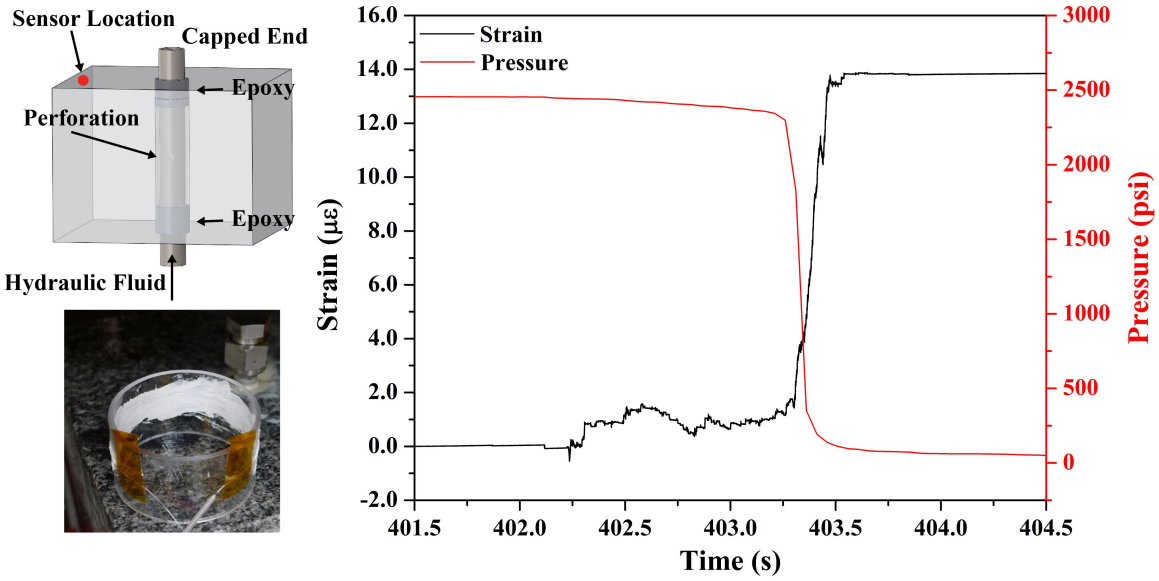


Figure 26: Strain versus time with reference to the applied hydraulic pressure; Inset: Schematic of the employed granite specimen for hydraulic fracturing and photo of the mounted fiber laser sensor on the specimen.

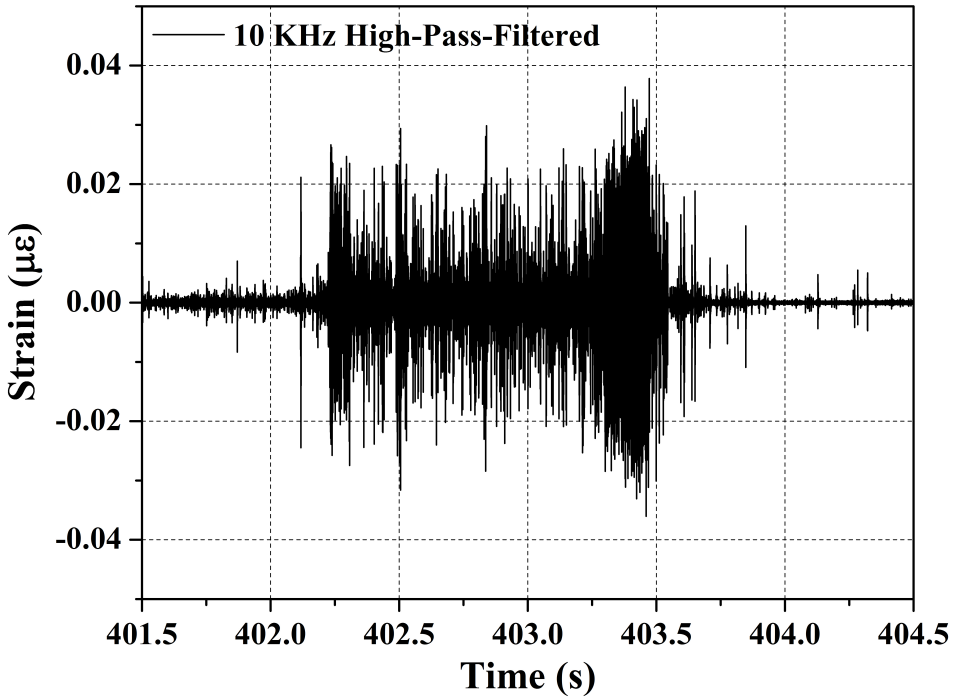


Figure 27: Strain measurement filtered by a 10-KHz high pass filter.

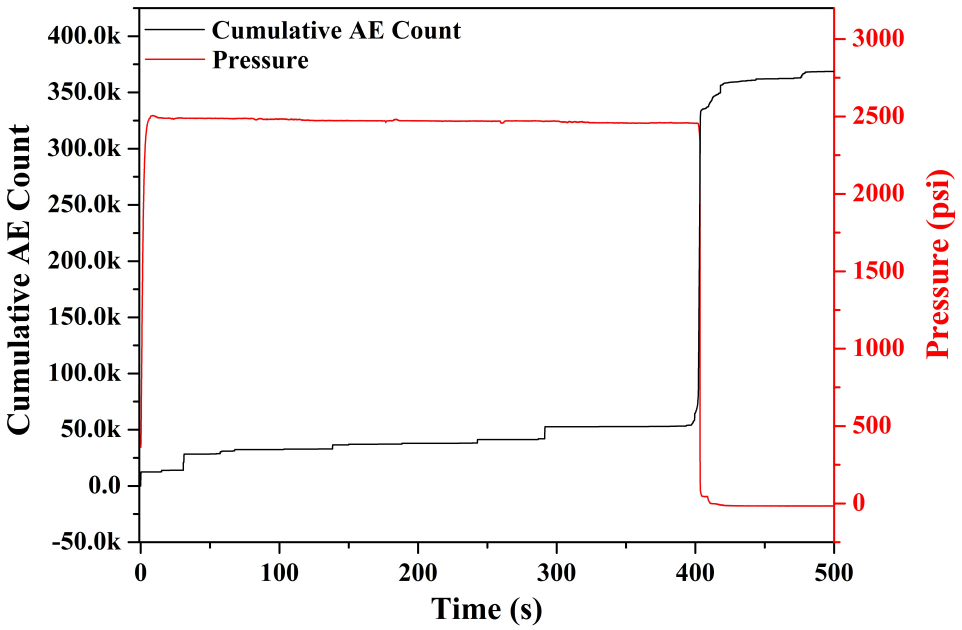


Figure 28: Cumulative AE count versus time with reference to the applied hydraulic pressure.

shown, the hydraulic fracture started to form right after the pressurization. More than 5 steps of count increase can be clearly identified implying over 5 times of hydraulic induced microscopic cracks were formed inside the specimen before the major breakdown. At ∼400 seconds, a significant step of AE count increase signals the onset of major fracture. The presented cumulative AE count is consistent with results obtained from a commercial PZT based AE system deployed onsite from MISTRAS.

# 6.0 3D STRAIN FIELD IMAGING USING RAYLEIGH SCATTER FOR HYDRAULIC FRACTURING MONITORING

## 6.1 OVERVIEW

In this chapter, a 3D strain imaging technique based on Rayleigh scattering OFDR method will be presented. This chapter gives the argumentation published in [74]. To effectively extract the internal strain field information, an optical fiber helix structure was embedded inside the sample during its casting process. The distributed axial strain along the optical fiber was then interrogated with 1-cm spatial resolution by using Rayleigh scattering OFDR. After coordinate conversion and data synthesizing, the axial strain measurements along the optical fiber in the helix structure were used to generate the 3D strain field images showing the strain distribution inside the sample. The proposed technique was verified in the field during the hydraulic fracturing tests. Thanks to those generated 3D strain field images, prediction of initial crack locations, monitoring of internal strain growth, and tracking of internally formed cracks were all demonstrated. Considering the almost unconstrained flexibility to embed different optical fiber imaging structures beside the helix demonstrated here, the proposed technique provides an innovative solution to effectively view the strain distribution and its evolution inside concrete samples in nearly arbitrary directions and locations.

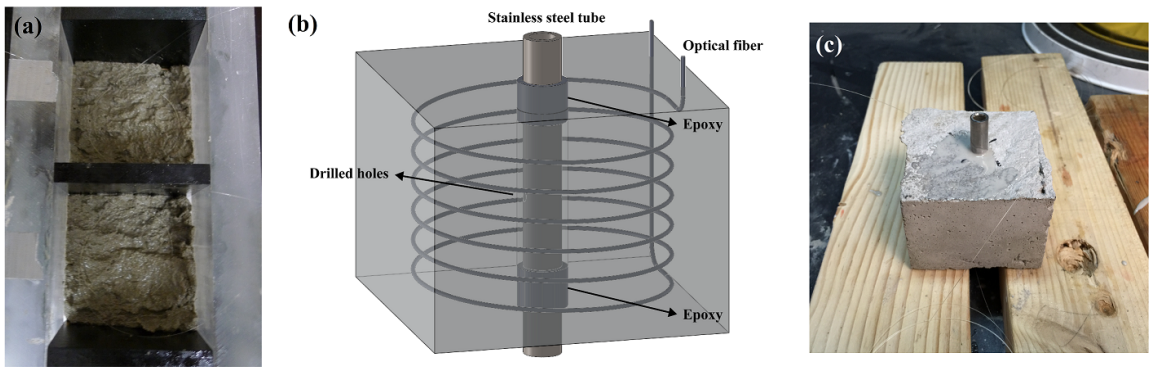


Figure 29: Photos taken (a) during the casting process and (c) after the concrete cube was fully prepared for hydraulic fracturing tests; and (b) the schematic of the optical fiber embedded sample.

## 6.2 SENSOR DESIGN AND EMBEDDING

To achieve the 3D strain field imaging for hydraulic fracturing study, the conventional single mode optical fiber (SMF-28) needs to be embedded into the concrete cube during its casting process. Since Rayleigh scatter based OFDR is only sensitive to axial strain along the optical fiber, a helix structure was employed to provide with us more dimensions of strain information inside the cube. As is shown in Fig. 29, the optical fiber with a total length of 1.30 m was fully embedded into a 57 cm $\times$ 75 cm $\times$ 75 cm concrete cube, comprised of 6 rings of optical fiber for 120 cm to form the helix and also a section of optical fiber link for $\sim$6 cm running from the top of the cube to its bottom.

The optical fiber embedding process commenced along with the concrete deposition layer by layer in a bottom-to-up fashion. In total, six layers of the optical fiber and seven layers of concrete was deposited alternatively such that every layer of the optical fiber was properly

sandwiched by two layers of the concrete. The circumferences of the six rings of optical fiber were controlled to be ∼20 cm with 1-cm accuracy and their centers were placed as close as possible to the central axis of the cube parallel to the to-be-inserted stainless steel tube, as illustrated in Fig. 29b. The control over the spacing between different layers of optical fiber was lacking from this procedure. Therefore dissection analysis after the final tests was always taken to identify the vertical location of every layer of the helix. After the optical fiber was embedded, the concrete cube was drilled and inserted with a stainless steel tube with an outer diameter of 0.95 cm and inner diameter of 0.70 cm. The spacing between the inserted tube and the wall of the drilled well was subsequently back filled in for about 1-cm deep with epoxy on both ends, as indicated in Fig. 29b as well. At this point, a sealed pressure chamber located roughly at the center of the concrete cube was formed by the outer wall of the stainless tube, the epoxy fillings on both sides and the inner wall of the well. With a pair of diagonally drilled holes on the stainless steel tube and a sealing cap mounted at the bottom end of the tube, the hydraulic fluids (Polyglycol) can be channeled into and pressurize the chamber. The hydraulics system employed in this experiment is able to precisely control the hydraulic pressure inside the cube from 500 psi up to over 3000 psi. The fully prepared concrete cubes were then left to set for 1 week before the hydraulic fracturing tests.

The OFDR system employed in this experiment, the OBR 4600 (Luna Technologies), was butt coupled to the optical fiber embedded into the concrete cube as the FUT. Detailed discussion on how the OFDR system works in strain sensing has already been covered in section 2.6. Therefore some conclusive statements and equations are directly used here. Using a scanning range of 41.94 nm and the group delay mismatch $t_d = 800ns$, the maximum interrogating length for the Rayleigh backscattered signals is ∼42 m with a spatial resolution

~20 m according to 2.35. After every scan, the OFDR system generates the Rayleigh backscattered signal in the time domain. Thus the section of interest on the FUT can be easily identified and located, where the optical fiber is embedded in the cube. The time domain Rayleigh backscattering signal is then piecewise transformed back into the frequency domain with a step size of 1 cm along the FUT. Cross correlation is subsequently applied to the corresponding reference and measurement spectra to quantify segmented spectra shifts. With 2.36, the distributed strain measurement is achieved with spatial resolution of 1 cm and accuracy of 1 $\mu\epsilon$.

## 6.3 DISTRIBUTED AXIAL STRAIN MEASUREMENTS AND 3D STRAIN FIELD IMAGING

Fig. 30 shows the distributed axial strain measurements for two concrete cubes, sample 1 and sample 2, tested in this experiment. The total lengths of the two FUTs shown in the figure are both ~130 cm which correspond to the actual lengths of optical fibers embedded inside the cubes. The two samples underwent the same fabrication procedure but were tested with different hydraulic fracturing conditions. The breakdown of sample 1 was induced by gradually increasing the hydraulic pressure inside the cube to where the catastrophic breakdown occurred. However, for sample 2, the hydraulic pressure was increased gradually at the beginning and then held at a critical pressure point, which was 1441 psi in this case, until the breakdown was observed. In Fig. 30a, the pressure induced strain along the embedded optical fiber was clearly observed and featured with 6 strain peaks whose periods were 20 cm. The strain along the FUT increased with the applied hydraulic pressure, which

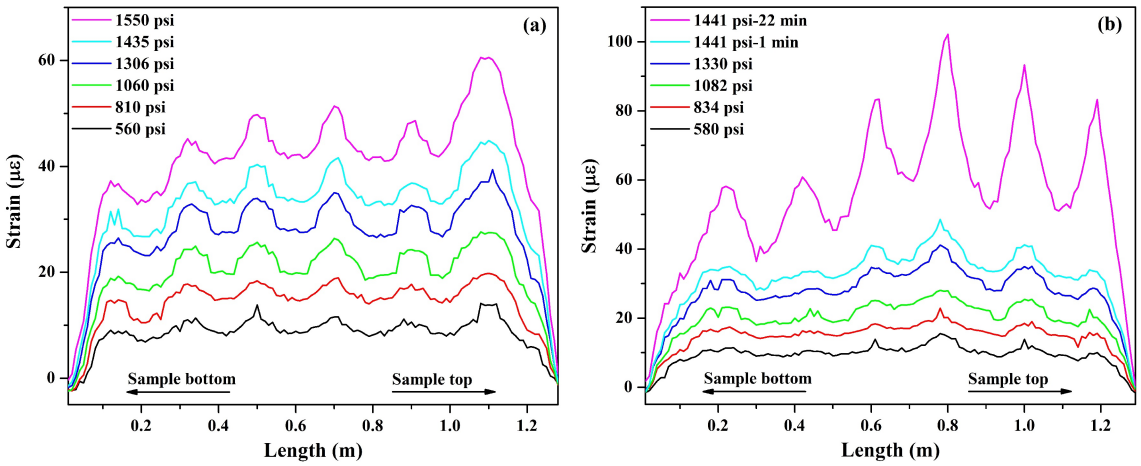


Figure 30: Distributed axial strain evolution of the embedded optical fibers in two concrete cubes. Different methods to induce the breakdown were employed (a) directly induced breakdown (b) delayed breakdown.

was directly indicative of the structural deformation of the cube. Such deformation increased slowly and evenly at the beginning of the pressurization from 560 psi to 1306 psi and then grew quickly into the final breakdown. It is also worth noting that the location corresponding to the last peak gained the strongest strain, indicative of the maximum displacement and namely the weakest spots in the cube. The following experiment results will show that the initial breakdown spot on the cube always prefers those weakest spots.

The distributed strain changes along the optical fiber embedded in sample 2 is shown in Fig. 30b. The strain growth behavior is rather similar to that of sample 1 since their initial pressurizing sequence is almost the same. But it is worth noting that the weakest spot appears to be located at the middle of the cube in this case. To induce delayed breakdown in sample 2, the hydraulic pressure was held at 1441 psi instead of further increased to 1550 psi.

Strain measurements were carried out every minute during this pressure maintaining period till the breakdown. The first and the last measurements in this session are shown in the Fig. 30b labeled as curve 1441 psi-1 min and 1441 psi-22 min, indicating the measurements is taken at 1 and 22 minutes after the hydraulic pressure is stabilized at 1441 psi. The catastrophic breakdown was observed in 5 seconds after the last measurement was taken. To further characterize the dynamics of strain growth, the strain evolution versus time curve obtained at the strongest strain peak is presented in Fig. 31. The peak strain grew slowly and evenly at the initial stage from 0 to 1100 s and then increased exponentially, as demonstrated by the curve fitting. It is important to note that such strain growth analysis can be carried out over any points across the 3D strain field images, only limited by the spatial resolution of the OFDR method.

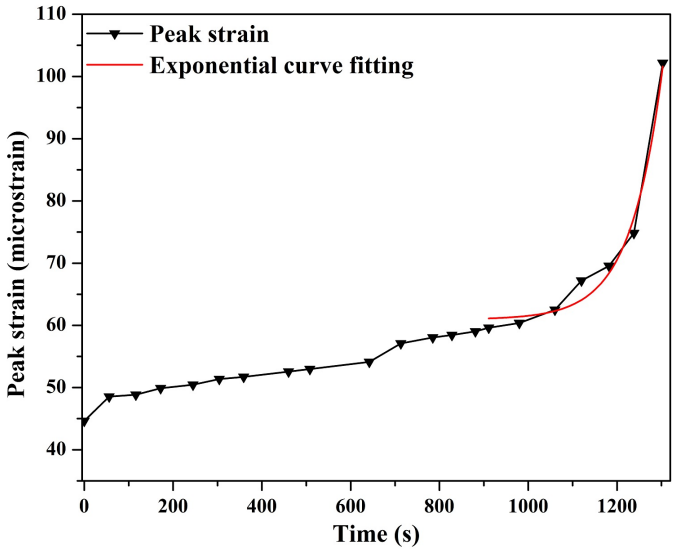


Figure 31: The strain evolution with time at a selected local point before the breakdown. The final stage of the strain growth is fitted by an exponential curve in red.

To better understand the physical meaning of the periodic strain peaks observed in the tests for both samples. The 3D strain field images were generated based on the distributed strain measurements. Given the total length of the optical fiber in the helix structure is ∼120 cm and the spatial resolution of the measurement is 1 cm, the helix structure consists of ∼120 strain data points in total. Those points can be mapped to 3D domain by converting their linear coordinates on the optical fiber to the corresponding spatial coordinates in the helix. To achieve this, the circumference of every ring in the helix structure was taken as exact 20 cm and the height information for each cycle of the optical fiber in the helix was measured by dissection carried out at the end of the test. The strain field images in 2D format are also provided to fully demonstrate the strain field information around the helix structure.

The reconstructed strain fields in 2D and 3D formats for sample 1 were shown in Fig. 32. The x, y and z axis in 3D format images form the spatial coordinate system for the concrete cube. The bottom face center of the cube is set at the origin of the 3D coordinate system. The 2D format can be visualized by unwrapping the 3D formant data into a plane and the unwrapping is done such that the optical fiber enters the helix shape at the bottom left corner of the 2D image and exits the structure at its top right corner. The actually formed helix structure has variable pitches measured in the dissection. Therefore the reconstructed 2D strain field does not result in a perfect parallelogram shape. As shown in the figure, the physical meaning of the strain peaks now appears clearly to be a localized strong strain band imaged on the side surface of the helix, which probably corresponds a potential vertical crack or strong displacement plane formed internally that runs from the central axis parallel to the inserted tube to a side face of the cube. Such internal crack plane intersects all six rings

in the helix structure vertically. This is the reason why the observed six strain peaks have almost the same interval that is equal to the circumference of the rings in the helix. It is clear that the strongest strain existed at the top of the cube, which was also where the actual breakdown initially occurred. In addition, the strain values at the bottom left shown in the 2D format are close to 0. It is indicative of the inaccuracy of the mapping method employed. Such inaccuracy is derived from a roughly 5-cm-long section of the optical fiber which is actually not in the helix but has been counted as part of that. The mapping inaccuracy can be readily resolved, provided through location measurement of the optical fiber embedded is available.

The strain field images in 2D and 3D formats for sample 2 are presented in Fig. 33. The most apparent difference from sample 1 is that the localized and radially distributed strong deformation plane was not formed until higher pressures were applied, i.e. 1441 psi. For comparison, in sample 1, the clear formation of the deformation plane showed up right after the cube was pressurized with only 560 psi. In sample 2, such feature only started to rise after 1082 psi and became apparent at 1441 psi, as demonstrated respectively in Fig. 30b and Fig. 30c. Since more hydraulic pressure was needed to develop the initial weakest spots, sample 2 was shown to have better resistance to induced hydraulic pressure. Moreover, barely one strain peak was apparently observable when 1441 psi was just applied and then the other periodic strain peaks started to grow out, which was also indicative of better structural integrity against the applied pressures. That is the reason why the radial deformation plane intersecting all 6 rings in the helix structure was not formed at the beginning of pressurization process. It is also worth noting that the weakest spot for sample 2 was located at the middle of the cube. The blue up-right corner shown in Fig. 33c and 33f

is due to the inaccuracy of the mapping method since the optical fiber corresponding to that section was actually out of the concrete cube.

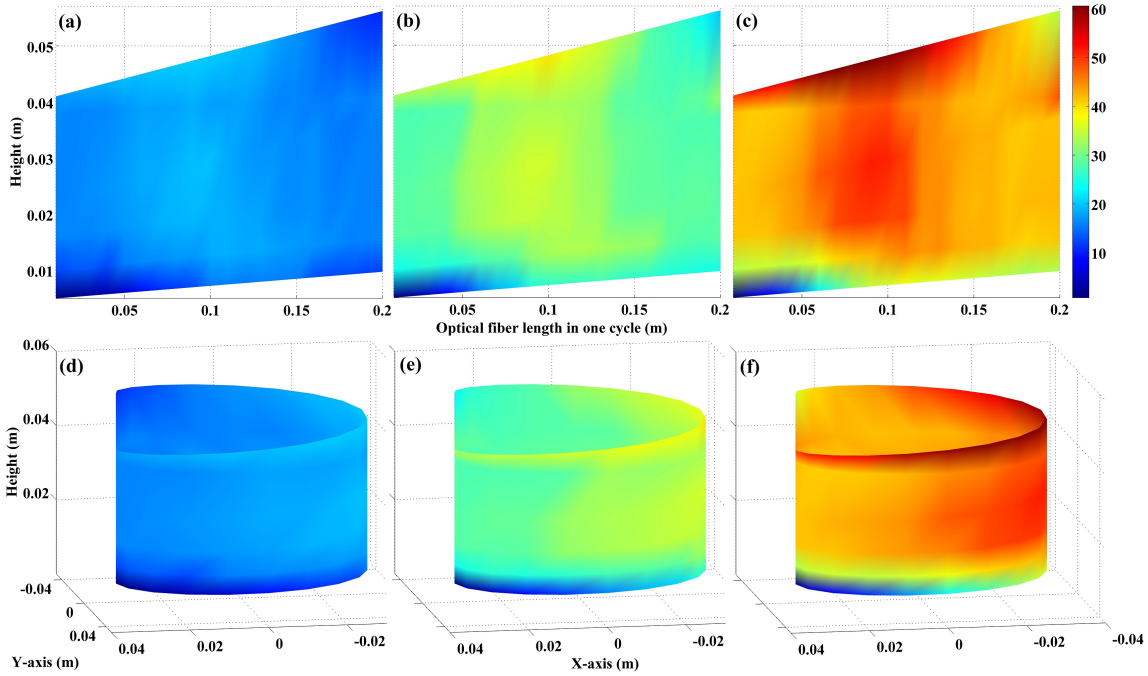


Figure 32: Reconstructed strain fields of the sample 1 in 2D (a ∼ c) and 3D (d ∼ f) formats under different pressure conditions 810 psi (a and d), 1306 psi (b and e), and 1550 psi (c and f).

After the hydraulic-induced breakdown, the optical fibers embedded in the concrete cubes were still functional except the significantly increased axial strain. Fig. 34 and Fig. 35 show the respective strain field images after the breakdown along with photos taken for the samples at the testing field. The typical strain values measured after the crack were readily on the orders of thousands of micro strains, denoting the onsite of catastrophic breakdowns. The localized and vertical deformation planes were still observed in both cases, which were believed to indicate the internal fracture shapes formed in the respective samples.

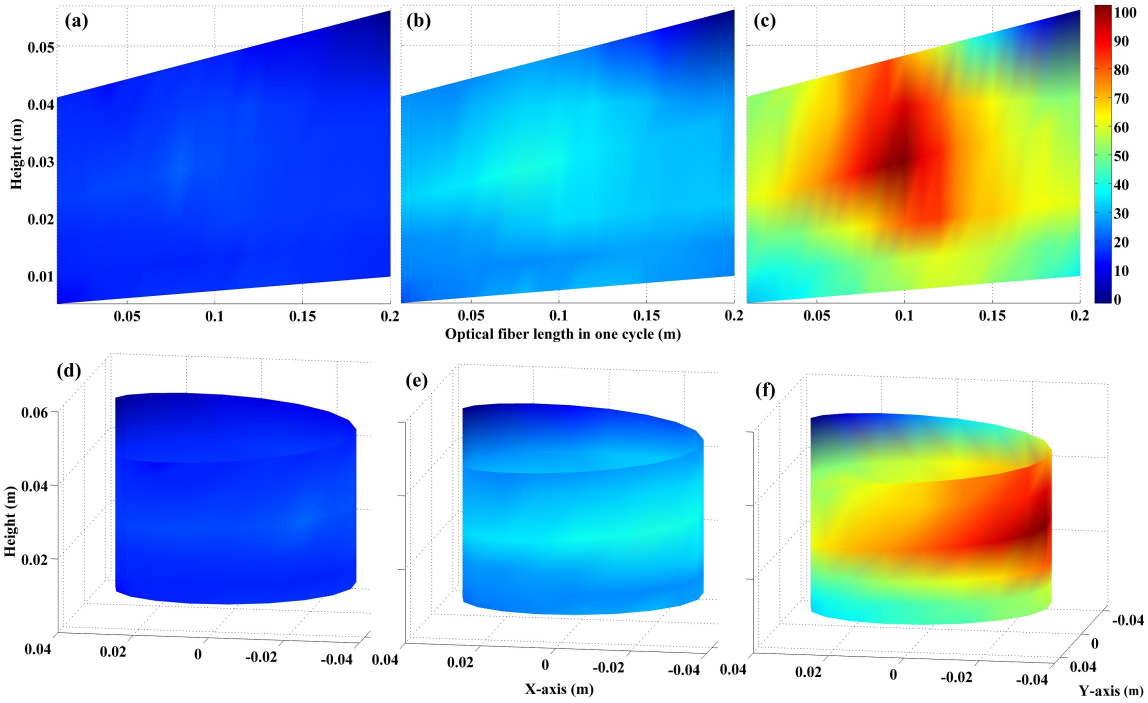


Figure 33: Reconstructed strain fields of the sample 2 in 2D (a $\sim$ c) and 3D (d $\sim$ f) formats under different pressure conditions 834 psi (a and d), 1330 psi (b and e), and 1441 psi-22 min (c and f).

Even though the actual fractures in sample 1 shifted from its location shown in the last measurement (Fig. 32c) after the breakdown, the position of the final fracture in sample 2 matched well with the last measurement (Fig. 33c). More importantly, as anticipated from the locations of the weakest spots shown in 3D strain field images, the corresponding initial locations for hydraulic fluid spill outs were observed at the top of the cube for sample 1 and in the middle of the cube for sample 2. The photos for both spill-out locations are shown in Fig. 34c and Fig. 35c.

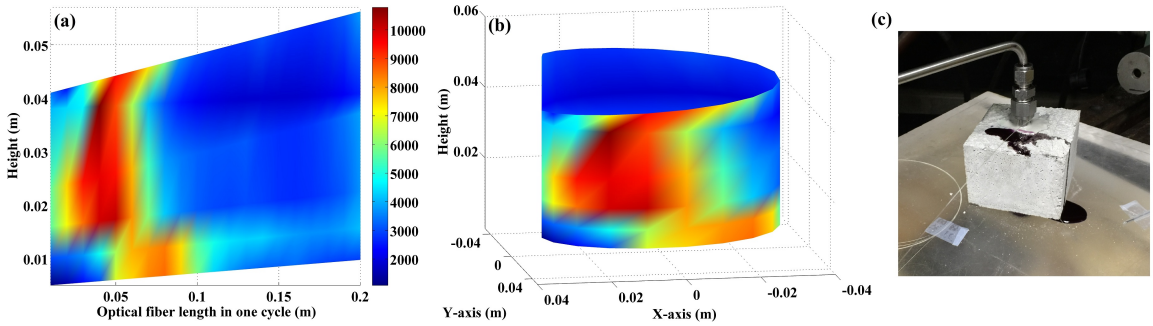


Figure 34: Strain field images in 2D (a) and 3D (b) format, and (c) the photo of the actual concrete sample 1 after the breakdown.

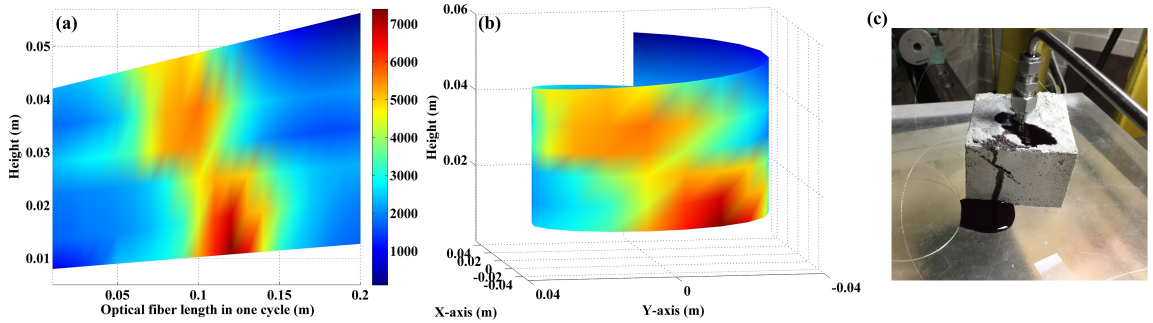


Figure 35: Strain field images in 2D (a) and 3D (b) format, and (c) the photo of the actual concrete sample 2 after the breakdown.

# 7.0 ACCURACY IMPROVEMENT OF RAYLEIGH OFDR USING CAVITY RING DOWN METHOD

## 7.1 OVERVIEW

In this chapter, continuing the Rayleigh OFDR system application involved in the previous chapter, we consider a method to improve the limit of detection (LOD) of the Rayleigh system. For the system employed, its intrinsic accuracy on detecting temperature or strain is on the level of $\pm 0.1\,^{\circ}\mathrm{C}$ and $\pm 1\mu\epsilon$. Such LOD performance is derived from the measurement uncertainty of the photo detectors employed in the OFDR system and as well the intrinsic noise out of cross correlation of Rayleigh spectra [75]. Out of those negative noise sources, the detection noises are believed to be random and stochastic, which can therefore be averaged out by repetitive measurements obtained simultaneously. Based on this concept, we proposed to use the cavity ring down (CRD) configuration to effectively reduce the random components in measurement noise of the OFDR system, therefore further enhancing its LOD.

Conventional CRD spectroscopy [76, 77] is a sensitive time domain technique that has been used in variety of optical sensing applications especially with the use of optical fibers, such as chemical composition determination [78], weak optical loss measurement [79] and refractive index measurement [80]. The working principle of it can be generalized that any

small attenuation of transmitted optical intensity in a high-finesse optical cavity can be interrogated by accumulating the losses by multiple times as optical intensity rings down the cavity. With such accumulation and ring down of pulse in time, a CRD time $\tau$ can be calculated which correlates the degradation rate of the light intensity with the measurement of interests. To compensate intrinsic cavity loss (fiber loss and fiber couplers insertion loss) in optical fiber cavities, EDFAs are usually used [81] to amplify the optical pulse per round trip. Although CRD technique has become a relatively mature methodology, the use of innovative in-fiber distributed measurement in tandem with CRD scheme has not yet been vastly explored. In 2014, Passos, Silva et al. firstly demonstrated the fiber CRD using an optical time-domain reflectometer (OTDR) [82, 83], where OTDR system was used as both the light source and the interrogation tool to measure in-fiber axial strain.

Through this chapter, we leveraged both the fiber CRD and the OFDR technique to explore the feasibility that with a single scan of the OFDR unit the same FUT could be interrogated by over 10 times to obtain on-fiber strain or temperature measurements. After averaging all the obtained measurements, reduction of system measurement noise for over 69% was achieved, which resulted in increase of LOD for the OFDR system.

## 7.2 SYSTEM CONFIGURATION

The system configuration is shown in Fig. 36. It comprises a commercial available Rayleigh OFDR system previously introduced in the section 2.6 and necessary components to form a ring cavity. A 80/20 fiber coupler is used as the light combining item, where CW laser emission from the OFDR unit is sent into the cavity via the 80% port. Then a section of

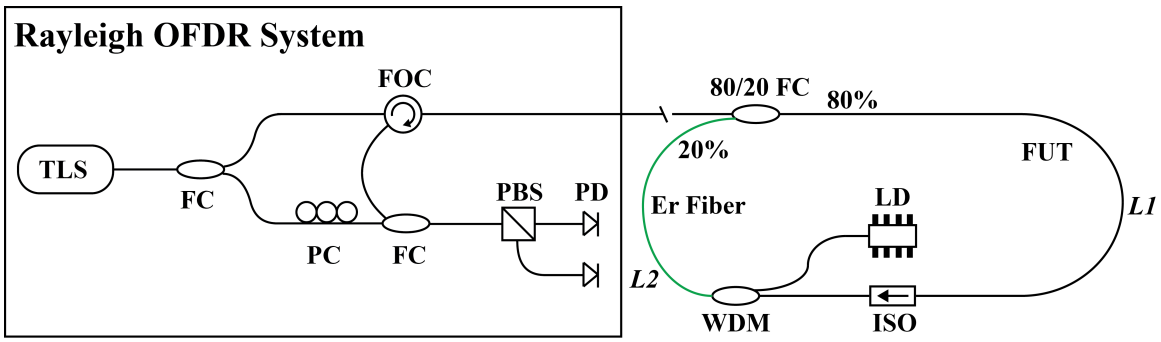


Figure 36: The schematic of the cavity ring down scheme for the Rayleigh OFDR. TLS: tunable laser source; FC: fiber coupler; PC: polarization controller; FOC: fiber optic circulator; PBS: polarizing beamsplitter; FUT: fiber under test; PD: photodetector; LD: laser diode; ISO: isolator; WDM: wavelength division multiplexer.

$\sim$2.33-m-long single mode fiber is employed as the FUT for either temperature or strain measurement. After that, an isolator is followed to rectify the light propagation in the optical cavity, based on which all the optical components forming a EDFA amplifier are made "invisible" to the OFDR interrogation, as long as the lengths of different sections of the optical fiber follow the mathematical expression below,

$$\begin{aligned} 2(L0+L1) &< L1+L2+L0+L0 \\ L1 &< L2 \end{aligned} \tag{7.1}$$

,where $L0$ is the length of optical fiber extending from the OFDR unit to the fiber coupler, $L1$ corresponds to the length of the FUT between the fiber coupler and the isolator, and $L2$ is responsible for the total length of optical fiber involved in forming the EDFA amplifier located between the isolator and the fiber coupler. This inequality (7.1) evaluates the spatial

distances of reflected Rayleigh signals of FUT belonged to different cycles of light ringing down the CRD cavity. When this inequality stands, the OFDR system is able to interrogate the full length of the FUT and their distributed Rayleigh signals are differentiable in spatial domain. On the other hand, if the condition does not stand, the reflected Rayleigh signals of the FUT belonged to different cycles would merge together, which prevents us from telling apart the Rayleigh signals from different cycles of the CRD trips. For this specific configuration, the intrinsic cavity loss is partially compensated by using a in-cavity EDFA. As shown in Fig. 36, the EDFA is composed of a high-power laser diode (JDSU S27 series with max power 460 mw), a WDM and a ∼3-meter-long Erbium doped optical fiber (Corning Er 1600 L3). The constructed EDFA was working under typical forward pumping configuration. To ring down the cavity, scanning laser emission from the OFDR unit is initially sent into the cavity via the 80/20 fiber coupler where it incurs ∼8 dB loss. Then the light passes through an isolator with insertion loss of ∼0.5 dB. Finally comes the EDFA unit, where optical loss accumulates in one cycle is partially compensated. After the amplifier, the light is sent back into the cavity again via the 20% port of the fiber coupler. When the optical field of OFDR unit just enters the cavity through the 80/20 coupler, in this initial cycle generated Rayleigh back scatter signals go back towards to the unit via the same path as the probing light comes. However, after the initial cycle, the way that generated Rayleigh back scatter signals propagate back to the OFDR unit does not follow the same fashion because of the employment of an isolator and its rectifying on light propagation. Instead, the Rayleigh signal passes the fiber coupler only once and propagates right back to the unit. Such differing behavior on how the OFDR system receives the back scattered Rayleigh signals lays down the founding mechanism for the inequality (7.1).

## 7.3 CAVITY RING DOWN AND ITS ENHANCEMENT ON THE SYSTEM LOD

In this section, we will discuss the spatial CRD formation interrogated with the OFDR and explore its enhancement on LOD for temperature and strain measurements of this system. In Fig. 37, the CRDs interrogated by the OFDR in the spatial domain is presented, where we respectively indicate the full interrogated length of the FUT from different CRD trips using # 1 to # 10 and the zeroth measurement (# 0) corresponds to the measured section of FUT not obtained with the CRD technique, namely the initial cycle, while in Fig. 38 we compare the same CRD configuration not using the EDFA. In comparison, in the first cycle of CRD, the EDFA boosted the light intensity for about ∼5.5 dB using a 300-mA 980-nm pumping power. The spatial resolution in these figures was set as $\sim 20\mu m$.

The most striking features in Fig. 37 are those periodic and sharp reflection peaks. Besides the reflection peak indicated and derived from the FC (fiber coupler) where probing light just enters the ring cavity, there are also periodic patterns entailing two reflection peaks and a reflection valley to form dividers between every adjacent Rayleigh back scatter signals of the FUT section in the spatial domain. For the formed periodic dividers, the first reflection peak is derived from the strong back reflection of probing light in the fiber optic isolator interfaces and the second peak is similarly due to the back reflection in the optical fiber coupler. The valley portion in the divider corresponds to the photodetector noise background level employed in this OFDR system. Based on the current CRD design, in the spatial domain and over the valley regions no back scattered Rayleigh signal can be received. The fiber optic isolator prevents any returned signal after its location. With the

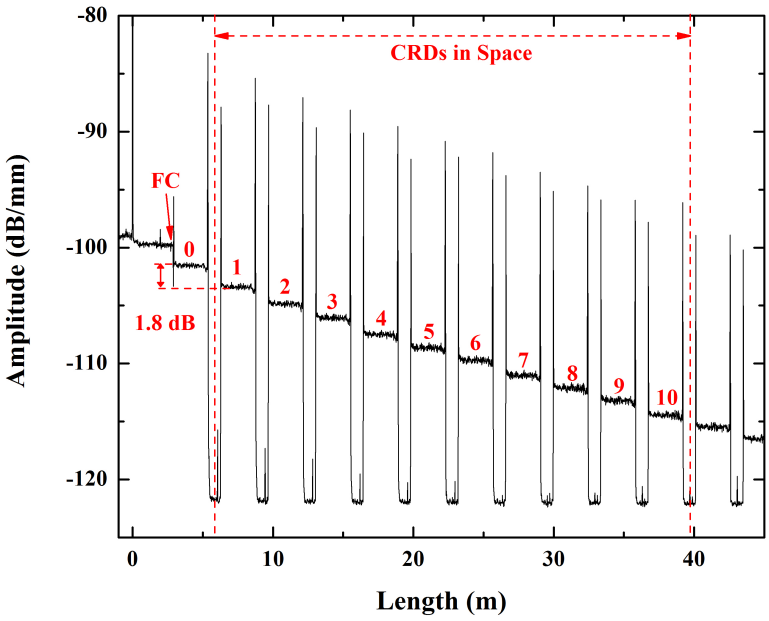


Figure 37: Interrogated CRD formation in spatial domain with EDFA applied. FC: fiber coupler.

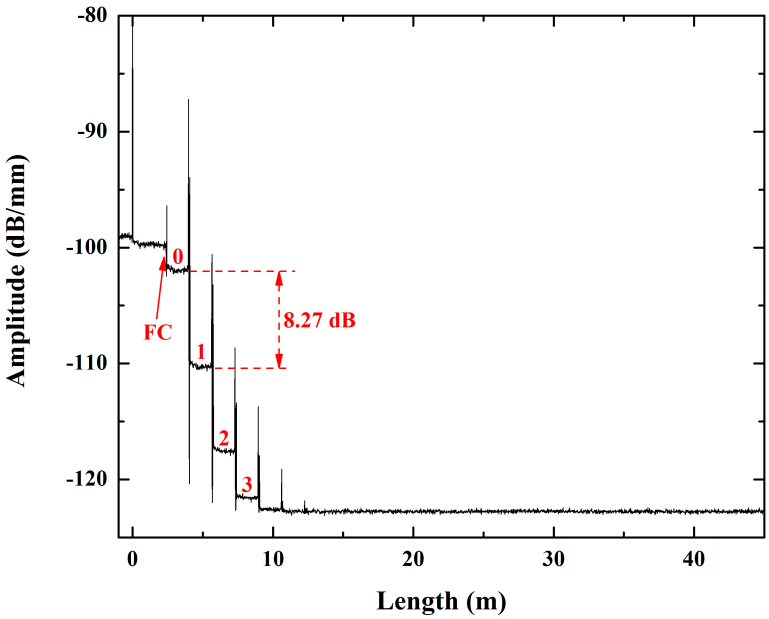


Figure 38: Interrogated CRD formation in spatial domain without using EDFA. FC: fiber coupler.

onset of those dividers, individual Rayleigh signals obtained from different cycles of the CRD would be easily differentiated. The length of this divider is equal to,

$$\begin{aligned} Ls &= (L0 + L0 + L2 + L1) - 2(L0 + L1)/2 \\ &= (L2 - L1)/2 \end{aligned} \tag{7.2}$$

, where $Ls$ corresponds to the length of the periodic divider and the denominator 2 is derived from the double pass nature of the light propagation in all reflectometry based systems. This equation (7.2) necessitates the inequality (7.1) presented previously. For the CRD configuration presented here, only when the inequality holds, the periodic divider is on site so that Rayleigh signals from different cycles of the CRD are differentiable. The second striking feature in Fig. 37 is the obvious step-down pattern in the back scattered Rayleigh signals. Such feature is due to the insufficient power compensation of the EDFA in every cycle of the CRD process.

Though it is still insufficient to fully compensate the in-cavity loss which is as large as ~8.27 dB per cycle mainly derived from the fiber coupler, the number of sustainable CRD cycles has been greatly increased to more than 10 times. In Fig. 37, the net cavity loss between adjacent cycles shows decreasing trend, indicative of increase of gain in the EDFA system. It is worth mentioning that the EDFA system employed is sufficiently pumped to induce intra-cavity laser operation at 1562 nm even when the CW probing light of the OFDR is also present in the cavity. This technique, namely automatic gain control, has been demonstrated to successfully stabilize the gain of the EDFAs [81] since the gain in a lasing loop is clamped at the threshold value. However, in our CRD application, a deviation from the aforementioned behavior was observed, where EDFA gain increased as the signal level

decreased when the probing light ringed down the cavity. It is believed to be related to the frequency scanning nature of the OFDR system and stabilizing laser operation is inside such scanning span (1545 nm - 1587 nm). During a laser scan, the stabilizing laser operation in the cavity was perturbed by the probing laser from the OFDR when both emission wavelengths were close, which compromises the gain clamping mechanism based on intra-cavity lasing.

After the CRD was formed, we began to investigate its capability to increase the LOD of the OFDR system statistically. The ∼2.33-m-long FUT was put under test, in which 40-cm-long section is put in an isolated environment where ambient temperature perturbation along the optical fiber is minimal and negligible. Two measurement schemes were used to demonstrate the performance enhancement on LOD and also its statistical nature. In the first measurement scheme, the CRD scheme was used, where the OFDR system was able to obtain 11 individual measurements (10 of 11 were from CRD technique) simultaneously. As shown in Fig. 37, the distributed Rayleigh signals from steps/CRD cycles # 0 to # 10 were used to measure the ambient temperatures. Namely, every extra cycle in which probing light propagated down in the cavity, one more temperature measurement was obtained. In our case, 10 extra measurements were taken into consideration. Such number of ring down times was chosen based on the spectral shift quality degradation rate due to the laser intensity drop as well as the time coherence degradation. To maintain faithful temperature/strain measurements, a larger than 0.90 spectral shit quality is considered sufficient (1 being the max value) and maintained till the last cycle of the CRD process contributing to the measurement. Then mean calculation was done to generate the averaged temperature profile around the specific isolated section. In the second measurement scheme, the OFDR was used under non-CRD configuration, where with every scan of the OFDR system a single

measurement was obtained. And we repeated the measurement process by extra 10 times to similarly mimic what the CRD configuration could do in one single scan statistically. Lastly mean calculation of all the 11 obtained measurements were carried out. In this scheme, we tried to produce a set of data that in statistical nature resembled our proposed CRD enhanced configuration.

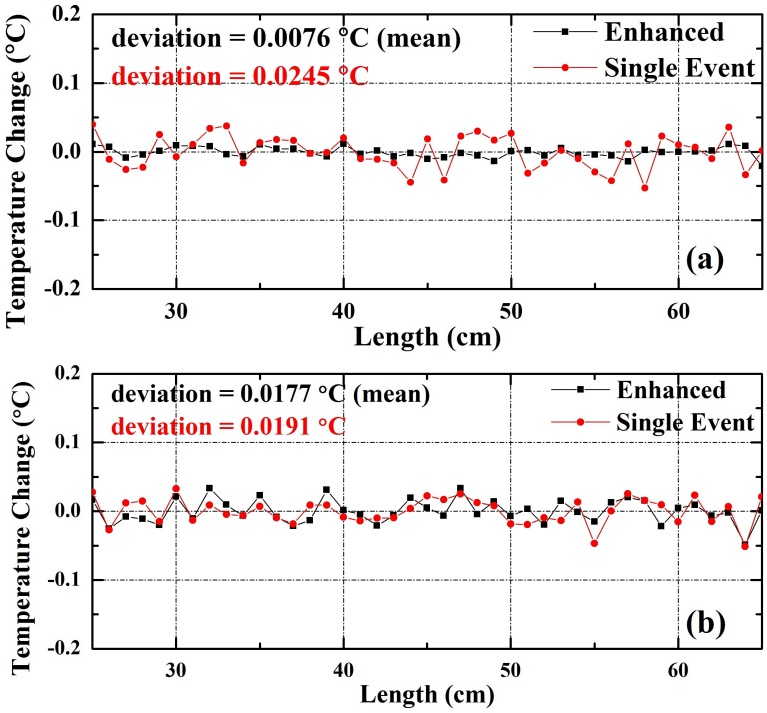


Figure 39: The 1st comparison of temperature measurements from (a) CRD enhanced configuration, and (b) statistically equivalent test sequence.

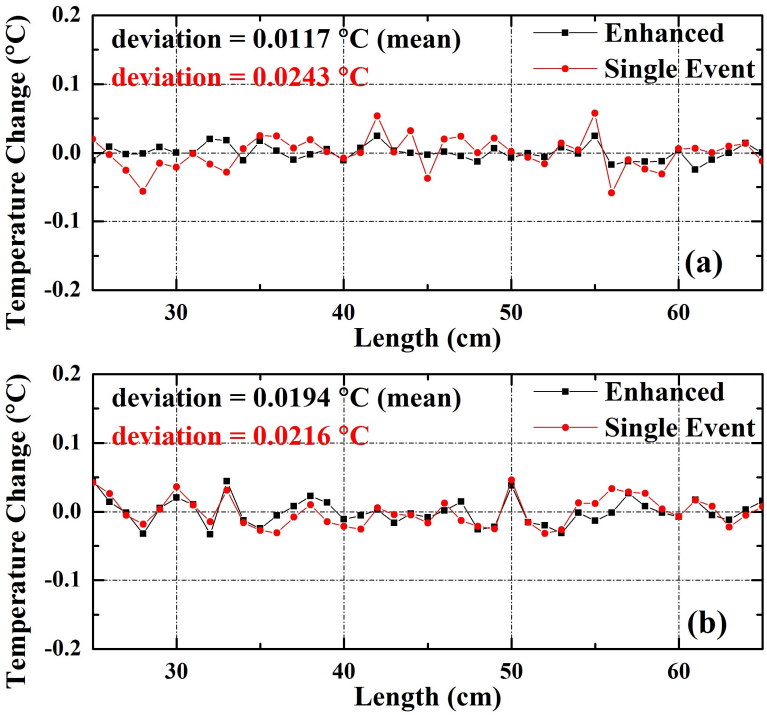


Figure 40: The 2nd comparison of temperature measurements from (a) CRD enhanced configuration, and (b) statistically equivalent test sequence.

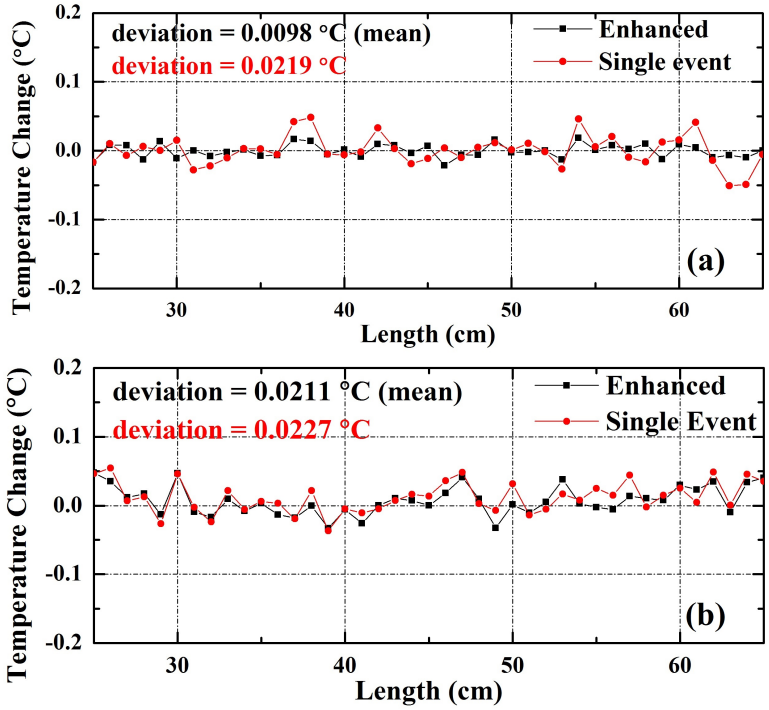


Figure 41: The 3rd comparison of temperature measurements from (a) CRD enhanced configuration, and (b) statistically equivalent test sequence.

In Fig. 39, Fig. 40, and Fig. 41, we present three pairs of individual temperature measurement results from our proposed CRD enhanced configuration and the other measurement scheme which resembles the CRD method in statistical nature. In Fig. 39a, Fig. 40a, and Fig. 41a, both curves are shown. The black curves correspond to the mean measurement over the same section of optical fiber enabled by the CRD configuration, while the red curves are from the initial cycle (step # 0 in Fig. 37) as probing light starts to ring down the cavity. In the other words, the red curves refer to single-event measurement like how the OFDR system is used conventionally. However, for Fig. 39b, Fig. 40b, and Fig. 41b, the measurement results were obtained through the statistically equivalent test sequences. In those figure, the black curves correspond to the average value from the 11 measurements while the red curves correspond to the first measurements in those respective sequences.

Out of the three comparison tests, the deviation for the black curves where CRD enhanced configuration is used varies from 0.0076 °C to 0.0117 °C, while the red curves regardless of the testing configuration employed give deviations ranging in 0.0191 °C to 0.0245 °C. By using CRD enhanced OFDR interrogation, the noise level has been reduced up to 69% with the minimum demonstrated reduction of 52%. Since all 11 measurements are taken almost at the same time and 1-cm long spatial resolution, the noise reduction is believed to be majorally associated with the reduction of detection noise of the OFDR system [75].

However, in Fig. 39b, Fig. 40b, and Fig. 41b, the supposedly statistically equivalent test scheme has only decreased the temperature deviation from 0.0191 °C to 0.0177 °C at the most. In this case, noise reduction of up to 7.3% is observed out of the three demonstrated tests. Such significant difference on noise level reduction capability is probably due to the time frame in which both schemes complete the data acquisition. For our proposed CRD

enhanced configuration, the measurement was done in less than 10 seconds however in the second scheme the process took more than 5 minutes. In this much larger time window and 11 subsequent measurements, lumped detection noises from the two individual photo detectors used in the Rayleigh OFDR system are believed to be larger in quantity in comparison with the CRD scenarios where only one time measurement is performed, resulting in the compromised noise reduction efficiency. We believe such difference in LOD improvement exactly signifies the practical value of our proposed CRD enhanced OFDR technique.

# 8.0 CONCLUSION AND FUTURE WORK

In conclusion, we have mainly investigated five sensing applications developed respectively for high-temperature extreme conditions and energy industrials. A high-temperature-stable DBR fiber laser was fabricated and characterized from the room temperature up to 750 °C (Chapter 3). The laser emission has been proved stable with power fluctuation of 1.06% for over 7 hours. Besides acting as a sustainable laser source and temperature gauge under high temperatures, the fiber laser and its fabrication techniques also show promising future to enable more fiber laser based sensing schemes usable under high temperature domains. One of the future work after this project should be the further development of high-temperature-resistant distributed feedback (DFB) fiber laser. DFB fiber lasers are well known for its high side mode suppression ratio and stable laser output, which are more significant than DBR fiber laser on telecommunication and even fiber sensing areas.

The second application covered in this thesis is a hot-wire flow meter intended to work up to 800 °C (Chapter 4). This is the highest operational temperature so far for a flow meter. Our demonstrated design has been calibrated for uninterpreted flow measurement from the room temperature up to 800 °C. The calibrated flow measurement range is 0.066 m/s to 0.66 m/s. Attributed to its high-temperature stability and all-optical-fiber construction, the sensor is believed to be ideal for some key industrial flow sensing needs such as down-hole

flow measurement for geothermal applications, high-temperature exhaust flow monitoring for fossil fuel energy industrials and also high-temperature liquid flow sensing for nuclear plants. One of the future work worth emphasizing is about exploring and developing the multiplexing and distributed sensing capability of the flow sensor, which can truly make the high-temperature flow sensor more versatile and valuable for practical industrial needs.

The third and fourth applications were both developed aiming at further enhancing the monitoring efficiency of hydraulic fracturing process for energy industrials. In chapter 5, the DFB fiber laser based strain sensor with proper mounting method was employed to detect acoustic emission events (AEs) during a in-lab fracturing process. Derived from the measured AE data, the plots of accumulated AE counts and instantaneous strain measured on the fiber sensor were provided. Based on the strain measurement plot,the DFB fiber laser sensor was shown with full capacity in pinpointing the induced fractures during the process, even those small cracks before any major breakdowns. Moreover, the plot of accumulated AE counts was served as a good counterpart for the similar plot generated with the PZT based transducers, in terms of functionality. The obtained results show that DFB fiber laser sensors are effective tools to monitor acoustic emission from hydraulic fracturing of laboratory specimens. As a highly multiplexed sensing technology, DFB fiber laser sensors offer an alternative to conventional PZT-based methods in monitoring fracturing processes for oil and gas industry.

In chapter 6, the fourth application presents the potential and feasibility to employ Rayleigh backscatter based OFDR technique in the field of hydraulic fracturing study. Derived from the 1 cm resolved distributed strain measurements along the fiber optic helix structure embedded in the concrete samples, internal 3D strain field images were formed.

The imaging techniques have been demonstrated rather effective to monitor the internal strain field evolution induced by the hydraulic pressures in 3D and also to anticipate initial crack locations. The optical fiber even survived the catastrophic breakdowns and therefore the internal fracturing shapes could still be imaged. This demonstrated application is believed to be an enabling technique that will open up new research possibilities and provide innovative findings possibly not only appreciated by the energy industrials concerning hydraulic fracturing but also other areas in the civil engineering community, such as structural health monitoring and defect detection. Future research efforts in this area include inventing other fiber imaging structure to elucidate specific civil engineering problems and also develop new mounting/ebedding techniques such that the presented imaging technique can be applied to other natural rocks.

The last chapter 7, we talked about an innovative method to enhance the LOD of a commercial OFDR system based on in-fiber Rayleigh scatter. For this type of system, its LOD is generally limited by two factors: system detection noises and noises intrinsic to cross correlation over random Rayleigh spectra during sensing. By quickly taking several measurements simultaneously, we can statistically reduce the random detection noises and therefore improve the system LOD. To achieve that, a fiber amplified CRD configuration was introduced to work in tandem with the Rayleigh OFDR system. With optical probing light ringing down the cavity, the OFDR system is able to differentiate the Rayleigh back scattered signals coming from different cycles in the ring-down process and therefore conducts repetitive temperature measurements with a single scan in less than ten seconds. Since all the repetitive measurements are acquired in this short period of time, system detection noises can be efficiently removed. In the three demonstrated measurements based on this

technique, we have achieved up to 69% noise level reduction, resulting in an improved LOD of the Rayleigh OFDR system. We expect this technique can add extra accuracy margin to the current Rayleigh scatter OFDR system for those sensing scenarios where system's inherent accuracy is barely enough.

## BIBLIOGRAPHY


[1] K. O. Hill, Y. Fujii, D. C. Johnson, and B. S. Kawasaki. Photosensitivity in optical fiber waveguides: Application to reflection filter fabrication. *Applied Physics Letters*, 32(10):647–649, 1978.

[2] Jacques Bures, Suzanne Lacroix, and Jean Lapierre. Réflecteur de bragg induit par photosensibilité dans une fibre optique: modèle de croissance et réponse en fréquence. *Appl. Opt.*, 21(19):3502–3506, Oct 1982.

[3] G. Meltz, W. W. Morey, and W. H. Glenn. Formation of bragg gratings in optical fibers by a transverse holographic method. *Opt. Lett.*, 14(15):823–825, Aug 1989.

[4] R. Kashyap, J.R. Armitage, R. Wyatt, S.T. Davey, and D.L. Williams. All-fibre narrowband reflection gratings at 1500 nm. *Electronics Letters*, 26(11):730–732, May 1990.

[5] P.J. Lemaire, R.M. Atkins, V. Mizrahi, and W.A. Reed. High pressure h2 loading as a technique for achieving ultrahigh uv photosensitivity and thermal sensitivity in geo2 doped optical fibres. *Electronics Letters*, 29(13):1191–1193, June 1993.

[6] P. Yeh. *Optical Waves in Layered Media*. Wiley Series in Pure and Applied Optics. Wiley, 2005.

[7] Yoshinori Hibino and Hiroaki Hanafusa. Defect structure and formation mechanism of drawing-induced absorption at 630 nm in silica optical fibers. *Journal of Applied Physics*, 60(5):1797–1801, 1986.

[8] Masami Kohketsu, Koichi Awazu, Hiroshi Kawazoe, and Masayuki Yamane. Photoluminescence in vad sio2 : Geo2 glasses sintered under reducing or oxidizing conditions. *Japanese Journal of Applied Physics*, 28(4R):622, 1989.

[9] Raman Kashyap. *Fiber bragg gratings*. Academic press, 1999.

[10] D. Grobnic, C.W. Smelser, S.J. Mihailov, R.B. Walker, and P. Lu. Fiber bragg gratings with suppressed cladding modes made in smf-28 with a femtosecond ir laser and a phase mask. *Photonics Technology Letters, IEEE*, 16(8):1864–1866, Aug 2004.

[11] C. W. Smelser, D. Grobnic, and S. J. Mihailov. Generation of pure two-beam interference grating structuresin an optical fiber with a femtosecond infrared source anda phase mask. *Opt. Lett.*, 29(15):1730–1732, Aug 2004.

[12] Christopher Smelser, Stephen Mihailov, and Dan Grobnic. Formation of type i-ir and type ii-ir gratings with an ultrafast ir laser and a phase mask. *Opt. Express*, 13(14):5377–5386, Jul 2005.

[13] P.G. Kazansky, P.S.J. Russell, and Hiromichi Takebe. Glass fiber poling and applications. *Lightwave Technology, Journal of*, 15(8):1484–1493, Aug 1997.

[14] X.C. Long and S.R.J. Brueck. Large-signal phase retardation with a poled electrooptic fiber. *Photonics Technology Letters, IEEE*, 9(6):767–769, June 1997.

[15] R. A. Myers, N. Mukherjee, and S. R. J. Brueck. Large second-order nonlinearity in poled fused silica. *Opt. Lett.*, 16(22):1732–1734, Nov 1991.

[16] K. O. Hill, B. Malo, F. Bilodeau, D. C. Johnson, and J. Albert. Bragg gratings fabricated in monomode photosensitive optical fiber by uv exposure through a phase mask. *Applied Physics Letters*, 62(10):1035–1037, 1993.

[17] Jean Martin, Jocelyn Lauzon, Simon Thibault, and Francois Ouellette. Novel writing technique of long and highly reflective in-fiber bragg gratings and investigation of the linearly chirped component. In *Conference on Optical Fiber Communication*, page PD29. Optical Society of America, 1994.

[18] J. Canning, M. Stevenson, J. Fenton, M. Aslund, and S. Bandyopadhyay. Strong regenerated gratings. *Proc. SPIE*, 7503:750326–750326–4, 2009.

[19] Bowei Zhang and M. Kahrizi. High-temperature resistance fiber bragg grating temperature sensor fabrication. *Sensors Journal, IEEE*, 7(4):586–591, April 2007.

[20] Somnath Bandyopadhyay, John Canning, Michael Stevenson, and Kevin Cook. Ultrahigh-temperature regenerated gratings in boron-codoped germanosilicate optical fiber using 193 nm. *Opt. Lett.*, 33(16):1917–1919, Aug 2008.

[21] S. Bandyopadhyay, J. Canning, P. Biswas, M. Stevenson, and K. Dasgupta. A study of regenerated gratings produced in germanosilicate fibers by high temperature annealing. *Opt. Express*, 19(2):1198–1206, Jan 2011.

[22] Eric Lindner, John Canning, Christoph Chojetzki, Sven Brückner, Martin Becker, Manfred Rothhardt, and Hartmut Bartelt. Post-hydrogen-loaded draw tower fiber bragg gratings and their thermal regeneration. *Appl. Opt.*, 50(17):2519–2522, Jun 2011.

[23] Tao Wang, Li-Yang Shao, John Canning, and Kevin Cook. Temperature and strain characterization of regenerated gratings. *Opt. Lett.*, 38(3):247–249, Feb 2013.

[24] Tong Chen, Rongzhang Chen, Charles Jewart, Botao Zhang, Kevin Cook, John Canning, and Kevin P. Chen. Regenerated gratings in air-hole microstructured fibers for high-temperature pressure sensing. *Opt. Lett.*, 36(18):3542–3544, Sep 2011.

[25] Yang Zhang, Bai-Ou Guan, and Hwa-Yaw Tam. Characteristics of the distributed bragg reflector fiber laser sensor for lateral force measurement. *Optics Communications*, 281(18):4619 – 4622, 2008.

[26] A.C.L. Wong, W.H. Chung, Chao Lu, and Hwa yaw Tam. Composite structure distributed bragg reflector fiber laser for simultaneous two-parameter sensing. *Photonics Technology Letters, IEEE*, 22(19):1464–1466, Oct 2010.

[27] Li-Yang Shao, Xinyong Dong, A.P. Zhang, Hwa yaw Tam, and Sailing He. High-resolution strain and temperature sensor based on distributed bragg reflector fiber laser. *Photonics Technology Letters, IEEE*, 19(20):1598–1600, Oct 2007.

[28] Yang Zhang and Bai ou Guan. High-sensitivity distributed bragg reflector fiber laser displacement sensor. *Photonics Technology Letters, IEEE*, 21(5):280–282, March 2009.

[29] Bo Liu and Hao Zhang. Polarimetric distributed bragg reflector fiber laser sensor array for simultaneous measurement of transverse load and temperature. *Optical Fiber Technology*, 17(6):619 – 625, 2011.

[30] Y. Lai, A. Martinez, I. Khrushchev, and I. Bennion. Distributed bragg reflector fiber laser fabricated by femtosecond laser inscription. *Opt. Lett.*, 31(11):1672–1674, Jun 2006.

[31] Nemanja Jovanovic, Mattias Åslund, Alexander Fuerbach, Stuart D. Jackson, Graham D. Marshall, and Michael J. Withford. Narrow linewidth, 100 w cw yb3+-doped silica fiber laser with a point-by-point bragg grating inscribed directly into the active core. *Opt. Lett.*, 32(19):2804–2806, Oct 2007.

[32] Yonghang Shen, Yanqing Qiu, Bo Wu, Weizhong Zhao, Shuying Chen, Tong Sun, and Kenneth T. V. Grattan. Short cavity single frequency fiber laser for in-situ sensing applications over a wide temperature range. *Opt. Express*, 15(2):363–370, Jan 2007.

[33] D.Yu. Stepanov, J. Canning, L. Poladian, R. Wyatt, G. Maxwell, R. Smith, and R. Kashyap. Apodized distributed-feedback fiber laser. *Optical Fiber Technology*, 5(2):209 – 214, 1999.

[34] J.L. Philipsen, M.O. Berendt, P. Varming, V.C. Lauridsen, J.H. Povlsen, J. Hubner, M. Kristensen, and B. Palsdottir. Polarisation control of dfb fibre laser using uv-induced birefringent phase-shift. *Electronics Letters*, 34(7):678–679, Apr 1998.

[35] Gary A. Miller, Gordon M. Flockhart, and Geoffrey A. Cranch. Reducing phase errors during the inscription process of distributed feedback fiber lasers. In *Conference on Lasers and Electro-Optics/International Quantum Electronics Conference*, page CThE6. Optical Society of America, 2009.

[36] G.A. Miller, G.M.H. Flockhart, and G.A. Cranch. Technique for correcting systematic phase errors during fibre bragg grating inscription. *Electronics Letters*, 44(24):1399–1400, November 2008.

[37] Edmon Chehura, Stephen W James, and Ralph P Tatam. A simple and wavelength-flexible procedure for fabricating phase-shifted fibre bragg gratings. *Measurement Science and Technology*, 21(9):094001, 2010.

[38] G.A. Cranch, G.M.H. Flockhart, and C.K. Kirkendall. Distributed feedback fiber laser strain sensors. *Sensors Journal, IEEE*, 8(7):1161–1172, July 2008.

[39] Gary A. Miller, Geoffrey A. Cranch, and Clay K. Kirkendall. High-performance sensing using fiber lasers. *Opt. Photon. News*, 23(2):30–36, Jan 2012.

[40] David J. Hill, Phillip J. Nash, David A. Jackson, David J. Webb, S. F. O'Neill, Ian Bennion, and Lin Zhang. Fiber laser hydrophone array. In *Proc. SPIE*, volume 3860, pages 55–66, 1999.

[41] L. Zhang, W. Zhang, and I. Bennion. *In-Fiber Grating Optic Sensors*. CRC Press, 2 edition, Mar 2008.

[42] M.D. Todd, G.A. Johnson, and C.C. Chang. Passive, light intensity-independent interferometric method for fibre bragg grating interrogation. *Electronics Letters*, 35(22):1970–1971, Oct 1999.

[43] D. A. Jackson, R. Priest, A. Dandridge, and A. B. Tveten. Elimination of drift in a single-mode optical fiber interferometer using a piezoelectrically stretched coiled fiber. *Appl. Opt.*, 19(17):2926–2929, Sep 1980.

[44] A. Dandridge, A.B. Tveten, and T.G. Giallorenzi. Homodyne demodulation scheme for fiber optic sensors using phase generated carrier. *Quantum Electronics, IEEE Journal of*, 18(10):1647–1653, Oct 1982.

[45] Yu-Hsiang Wang, Chang-Pen Chen, Chih-Ming Chang, Chia-Pin Lin, Che-Hsin Lin, Lung-Ming Fu, and Chia-Yen Lee. Mems-based gas flow sensors. *Microfluidics and Nanofluidics*, 6(3):333–346, 2009.

[46] Gerald D Byrne, Stephen W James, and Ralph P Tatam. A bragg grating based fibre optic reference beam laser doppler anemometer. *Measurement Science and Technology*, 12(7):909, 2001.

[47] O. Frazao, P. Caldas, F. M. Araújo, L. A. Ferreira, and J. L. Santos. Optical flowmeter using a modal interferometer based on a single nonadiabatic fiber taper. *Opt. Lett.*, 32(14):1974–1976, Jul 2007.

[48] David W. Lamb and Adam Hooper. Laser-optical fiber bragg grating anemometer for measuring gas flows: application to measuring the electric wind. *Opt. Lett.*, 31(8):1035–1037, Apr 2006.

[49] H. H. Bruun. *Hot-Wire Anemometry: Principles and Signal Analysis*. Oxford University Press, 1995.

[50] L.J. Cashdollar and K.P. Chen. Fiber bragg grating flow sensors powered by in-fiber light. *Sensors Journal, IEEE*, 5(6):1327–1331, Dec 2005.

[51] Charles Jewart, Ben McMillen, Sung Kwon Cho, and Kevin P. Chen. X-probe flow sensor using self-powered active fiber bragg gratings. *Sensors and Actuators A: Physical*, 127(1):63 – 68, 2006.

[52] Paulo Caldas, Pedro A. S. Jorge, Gaspar Rego, Orlando Fraz ao, José Luís Santos, Luís Alberto Ferreira, and Francisco Araújo. Fiber optic hot-wire flowmeter based on a metallic coated hybrid long period grating/fiber bragg grating structure. *Appl. Opt.*, 50(17):2738–2743, Jun 2011.

[53] Xinhuai Wang, Xinyong Dong, Yan Zhou, Kai Ni, Jia Cheng, and Zhemin Chen. Hot-wire anemometer based on silver-coated fiber bragg grating assisted by no-core fiber. *Photonics Technology Letters, IEEE*, 25(24):2458–2461, Dec 2013.

[54] Shaorui Gao, A. Ping Zhang, Hwa-Yaw Tam, L. H. Cho, and Chao Lu. All-optical fiber anemometer based on laser heated fiber bragg gratings. *Opt. Express*, 19(11):10124–10130, May 2011.

[55] Tong Chen, Qingqing Wang, Botao Zhang, Rongzhang Chen, and Kevin P. Chen. Distributed flow sensing using optical hot -wire grid. *Opt. Express*, 20(8):8240–8249, Apr 2012.

[56] Marc Nikles and Fabien Ravet. Distributed fibre sensors: Depth and sensitivity. *Nat Photon*, 4(7):431–432, July 2010.

[57] Stephen T. Kreger, Dawn K. Gifford, Mark E. Froggatt, Brian J. Soller, and Matthew S. Wolfe. High resolution distributed strain or temperature measurements in single- and multi-mode fiber using swept-wavelength interferometry. In *Optical Fiber Sensors*, page ThE42. Optical Society of America, 2006.

[58] Robert R J Maier, William N MacPherson, James S Barton, Scott McCulloch, and Benjamin J S Jones. Distributed sensing using rayleigh scatter in polarization-maintaining

fibres for transverse load sensing. *Measurement Science and Technology*, 21(9):094019, 2010.

[59] Brian Soller, Dawn Gifford, Matthew Wolfe, and Mark Froggatt. High resolution optical frequency domain reflectometry for characterization of components and assemblies. *Opt. Express*, 13(2):666–674, Jan 2005.

[60] Mark Froggatt and Jason Moore. High-spatial-resolution distributed strain measurement in optical fiber with rayleigh scatter. *Appl. Opt.*, 37(10):1735–1740, Apr 1998.

[61] W. Eickhoff and R. Ulrich. Optical frequency domain reflectometry in single - mode fiber. *Applied Physics Letters*, 39(9):693–695, 1981.

[62] A.K. Sang, M.E. Froggatt, D.K. Gifford, S.T. Kreger, and B.D. Dickerson. One centimeter spatial resolution temperature measurements in a nuclear reactor using rayleigh scatter in optical fiber. *Sensors Journal, IEEE*, 8(7):1375–1380, July 2008.

[63] Rongzhang Chen, Aidong Yan, Mingshan Li, Tong Chen, Qingqing Wang, John Canning, Kevin Cook, and Kevin P. Chen. Regenerated distributed bragg reflector fiber lasers for high-temperature operation. *Opt. Lett.*, 38(14):2490–2492, Jul 2013.

[64] N. Kagi, A. Oyobe, and K. Nakamura. Temperature dependence of the gain in erbium-doped fibers. *Lightwave Technology, Journal of*, 9(2):261–265, Feb 1991.

[65] Rongzhang Chen, Aidong Yan, Qingqing Wang, and Kevin P. Chen. Fiber-optic flow sensors for high-temperature environment operation up to 800°c. *Opt. Lett.*, 39(13):3966–3969, Jul 2014.

[66] Kerstin Avila, David Moxey, Alberto de Lozar, Marc Avila, Dwight Barkley, and Bjorn Hof. The onset of turbulence in pipe flow. *Science*, 333(6039):192–196, 2011.

[67] S Takagi. A hot-wire anemometer compensated for ambient temperature variations. *Journal of Physics E: Scientific Instruments*, 19(9):739, 1986.

[68] Micheal B. Smith Carl T. Montgomery. Hydraulic fracturing: History of an enduring technology. *Journal of Petroleum Technology*, 62(12), December 2010.

[69] Tsuyoshi Ishida. Acoustic emission monitoring of hydraulic fracturing in laboratory and field. *Construction and Building Materials*, 15(5 - 6):283 – 295, 2001. Fracture Mechanics and Acoustic Emmission.

[70] B. D. Thompson, R. P. Young, and D. A. Lockner. Premonitory acoustic emissions and stick-slip in natural and smooth-faulted westerly granite. *Journal of Geophysical Research: Solid Earth*, 114(B2), 2009. B02205.

[71] Rongzhang Chen, Aidong Yan, Mohamed Zaghloul, Guanyi Lu, Andrew P. Bunger, Gary A. Miller, Geoffrey Cranch, and Kevin P. Chen. Monitoring of hydraulic fracturing using dfb fiber laser acoustic sensors. In *CLEO: 2015*, page STh4O.4. Optical Society of America, 2015.

[72] S.E.U. Lima, O. Frazao, R.G. Farias, F.M. Araujo, L.A. Ferreira, J.L. Santos, and V. Miranda. Mandrel-based fiber-optic sensors for acoustic detection of partial discharges - a proof of concept. *Power Delivery, IEEE Transactions on*, 25(4):2526–2534, Oct 2010.

[73] Qi Wu and Yoji Okabe. High-sensitivity ultrasonic phase-shifted fiber bragg grating balanced sensing system. *Opt. Express*, 20(27):28353–28362, Dec 2012.

[74] Rongzhang Chen, Mohamed A. S. Zaghloul, Aidong Yan, Shuo Li, Guanyi Lu, Brandon C. Ames, Navid Zolfaghari, Andrew P. Bunger, Ming-Jun Li, and Kevin P. Chen. High resolution monitoring of strain fields in concrete during hydraulic fracturing processes. *Opt. Express*, 24(4):3894–3902, Feb 2016.

[75] Sabastien Loranger, Mathieu Gagne, Victor Lambin-Iezzi, and Raman Kashyap. Rayleigh scatter based order of magnitude increase in distributed temperature and strain sensing by simple uv exposure of optical fibre. *Scientific Reports*, 5:11177–, June 2015.

[76] Giel Berden, Rudy Peeters, and Gerard Meijer. Cavity ring-down spectroscopy: Experimental schemes and applications. *International Reviews in Physical Chemistry*, 19(4):565–607, 2000.

[77] Kevin K. Lehmann, Giel Berden, and Richard Engeln. *An Introduction to Cavity Ring-Down Spectroscopy*, pages 1–26. John Wiley & Sons, Ltd, 2010.

[78] Helen Waechter, Jessica Litman, Adrienne H. Cheung, Jack A. Barnes, and Hans-Peter Loock. Chemical sensing using fiber cavity ring-down spectroscopy. *Sensors*, 10(3):1716, 2010.

[79] George Stewart, Kathryn Atherton, Hongbo Yu, and Brian Culshaw. An investigation of an optical fibre amplifier loop for intra-cavity and ring-down cavity loss measurements. *Measurement Science and Technology*, 12(7):843, 2001.

[80] N. Ni, C. C. Chan, L. Xia, and P. Shum. Fiber cavity ring-down refractive index sensor. *IEEE Photonics Technology Letters*, 20(16):1351–1353, Aug 2008.

[81] George Stewart, Kathryn Atherton, and Brian Culshaw. Cavity-enhanced spectroscopy in fiber cavities. *Opt. Lett.*, 29(5):442–444, Mar 2004.

[82] D. J. Passos, S. O. Silva, J. R. A. Fernandes, M. B. Marques, and O. Frazão. Fiber cavity ring-down using an optical time-domain reflectometer. *Photonic Sensors*, 4(4):295–299, 2014.

[83] S. Silva, D. J. Passos, M. B. Marques, and O. Frazao. Fiber cavity ring-down for strain sensing using an otdr. In *Photonics Conference, 2014 Third Mediterranean*, pages 1–3, May 2014.